

# Neutron optics of the PSI ultracold neutron source: characterization and simulation

G. Bison<sup>1</sup>, B. Blau<sup>1</sup>, M. Daum<sup>1</sup>, L. Göltl<sup>1</sup>, R. Henneck<sup>1</sup>, K. Kirch<sup>1,2</sup>, B. Lauss<sup>1,a</sup>, D. Ries<sup>1,2,b</sup>, P. Schmidt-Wellenburg<sup>1</sup>,  
G. Zsigmond<sup>1,c</sup>

<sup>1</sup> Paul Scherrer Institut, CH-5232 Villigen-PSI, Switzerland

<sup>2</sup> ETH Zürich, Zürich, Switzerland

July 15, 2019

**Abstract** The ultracold neutron (UCN) source at the Paul Scherrer Institute serves mainly experiments in fundamental physics. High UCN intensities are the key for progress and success in such experiments. A detailed understanding of all source parameters is required for future improvements. Here we present the UCN source components, elements of the neutron optics, the characterization of important related parameters like emptying times, storage times or transmission probabilities of UCN which are ultimately defining the UCN intensity delivered at the beamports. We also introduce a detailed simulation model of the PSI UCN source, used to analyze the measurements and to extract surface parameters.

**PACS.** 28.20.-v – 29.25.dz – 29.40.-Mc – 61.80.Hg

---

<sup>a</sup> Corresponding author, tel. +41(0)56 3104647, bernhard.lauss@psi.ch, ucn.web.psi.ch

<sup>b</sup> present address: Institute for Nuclear Chemistry, Johannes-Gutenberg-University, Mainz, Germany

<sup>c</sup> Corresponding author, tel. +41(0)56 3103569, geza.zsigmond@psi.ch, ucn.web.psi.ch

## 1 Introduction

Neutrons with velocities below about 8 m/s and hence with kinetic energies below about 300 neV, equivalent to temperatures below 3 mK are termed ultracold neutrons (UCN). Such neutrons have unique properties [1,2]. Most prominently, UCNs are reflected under any angle of incidence from suitable materials like steel, beryllium, nickel, diamond-like carbon (DLC) or nickel-molybdenum (NiMo). Hence, UCNs can be stored in bottles made from or coated with these materials, where they can be observed for hundreds of seconds, in principle only limited by the neutron lifetime. Moreover, UCN can also be guided to remote areas over tens of meters and behave more comparable to an extremely dilute ideal gas than to a particle beam. The specific description of UCN transport includes basic transport processes and includes also magnetic interactions, various loss mechanisms and gravity. All together can be summarized with the term UCN optics [3].

The distinct behavior makes UCN an ideal tool to study the intrinsic properties of the neutron and also to search for physics beyond the Standard Model of particle physics (BSM), most prominently represented by experiments searching for a possible permanent electric dipole moment of the neutron (nEDM) [4–10] or the precise determination of the neutron lifetime [11–14].

Such precision measurements are presently limited by neutron counting statistics, hence there are worldwide efforts to build new UCN sources with higher intensities [15,16]. A new high-intensity UCN source was designed and constructed at the Paul Scherrer Institute (PSI), Villigen, Switzerland, and started operation in 2011. Specific details and efforts were already reported in Refs. [16–24].

Here we compare source characterization measurements to detailed Monte-Carlo (MC) simulations using the simulation tool MCUCN [25] developed at PSI. This provides input to a better understanding of the UCN source performance.

Further increase of UCN intensities requires an excellent understanding of all components of the UCN source. Scope of the presented Monte-Carlo analysis is the extraction of parameters as defined in established UCN physics in order to characterize the quality of the optical components, and to identify possible improvements. For this purpose, all processes which could lead to a loss of UCN have to be identified, monitored and eliminated or reduced as much as possible. For instance, losses due to frost formation on the solid deuterium (sD<sub>2</sub>) surface have been only recently identified together with a way to recover performance [26].

This paper is organized in the following way. In Sec. 2 we give an introduction to all setup items of the UCN source which are relevant to its neutron optics performance. Section 3 provides an introduction to our simulation model describing the UCN transport in the source and its guides. In Sec. 4 we describe measurements which provide a

characterization of different important neutron optics parameters of the operating UCN source. Simulations used for the analysis of characterizing parameters are described in Sec. 5, followed by short conclusions in Sec. 6.

## 2 UCN source setup

Overviews of the main parts of the UCN source relevant to this work are shown in Figures 1 and 2. Many important subsystems devoted to cooling and cryo-operation [27], vacuum, gas handling, heavy water system, spallation target [28, 29] and the proton beam line [17, 30] are omitted here.

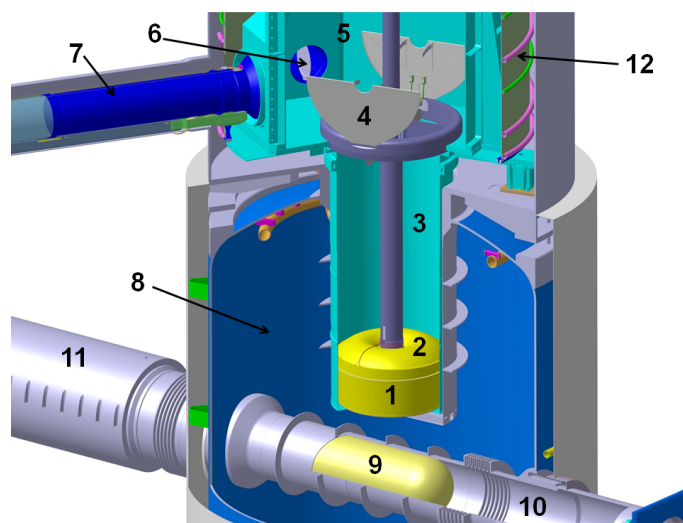


**Figure 1.** CAD image of the lower section of the UCN tank with indicated parts relevant to UCN production and transport (see text). 1 -  $D_2$  moderator vessel, 2 - lid, 3 - vertical guide, 4 - storage vessel flapper valve, 5 - storage vessel, 6 - UCN guide shutter, 7 - UCN guide section, 8 - heavy water moderator tank, 9 - spallation target, 10 - proton beam tube, 11 - target shielding, 12 - thermal shield.

The source operation is as follows: The full proton beam of 590 MeV and up to 2.4 mA is directed onto a spallation target [29] with a pulse length of up to 8 s. About 8 free neutrons per incident proton are produced in the target made of lead [31]. These neutrons are thermalized in the surrounding heavy water ( $D_2O$ ) at room temperature (about  $30^\circ C$  during operation). Thermal neutrons are further moderated and down-scattered into the cold and ultra-cold range inside solid deuterium ( $sD_2$ ), kept at a temperature of 5 K inside the moderator vessel located about 40 cm above the spallation target. UCN production in  $sD_2$  has been investigated over many years [32–44].

UCN leaving the  $sD_2$  gain kinetic energy by the material optical potential of 102 neV [45]. The UCN traverse a 0.5 mm thin AlMg3 lid separating the  $sD_2$  from the UCN storage vacuum. They are further guided upwards through a flapper valve into the storage vessel. At the end of the proton beam pulse the valve is closed and reopened about 20 s before the next pulse.

On the bottom of the storage vessel two UCN guides, called “West1” and “South”, connect the source to the corresponding beamports and experimental areas, West and South. Figure 2 shows a CAD image of this guide arrangement. The upper guide, “West-2”, with lower intensity is used for test measurements. Neutron shutters are positioned at the storage vessel exits and allow to close the vessel for UCN storage.

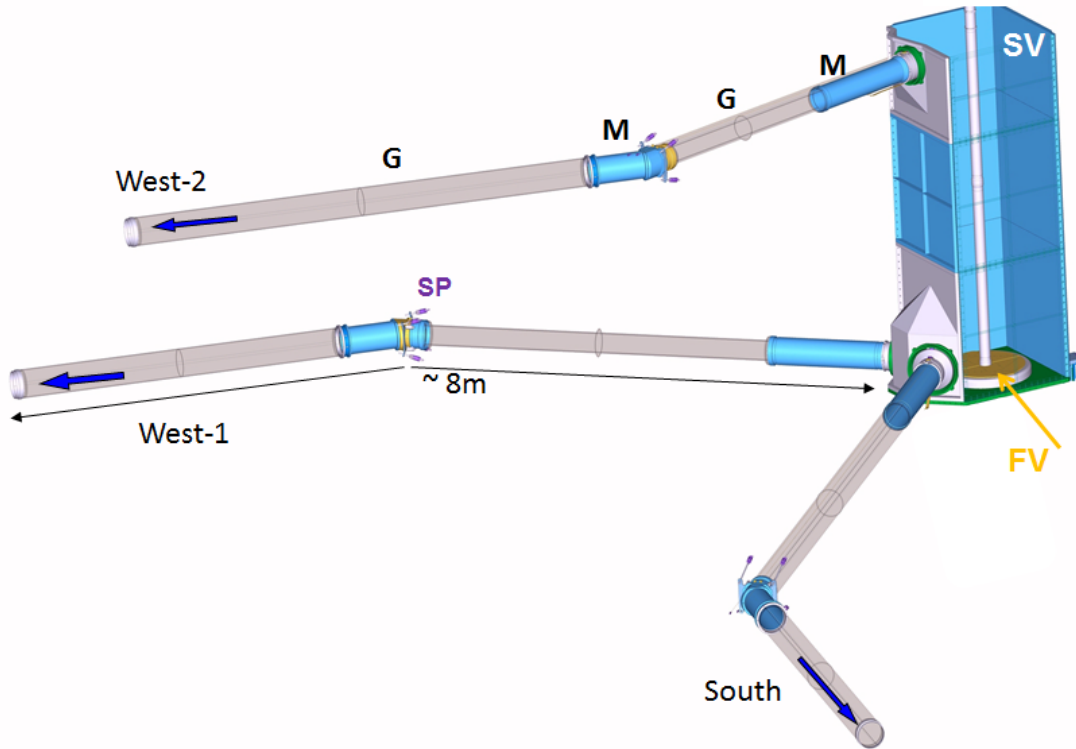


**Figure 2.** View of the three UCN guides and UCN storage vessel (SV) with closed flapper valve (FV). UCN guides made from glass tubes (G) are shown in light gray, metal tubes (M) are shown in darker blue, as indicated on guide West-1. Mechanical springs (SP) keep the positioning. The length of the UCN guide West-1 from SV to area West is approximately 8 m.

Proton beam operation for UCN production consists of single pulses of up to 8 s duration with a typical repetition period of 300 s. The maximum pulse length results from the constraint to keep the temperature rise inside the  $sD_2$  within a few Kelvin during the pulse. A kicker magnet was specially designed to allow for a fast kick of the full proton intensity to the UCN proton beamline with a rise and fall time of 2.5 ms [30]. A typical pulse sequence during standard operation is sketched in Fig. 3 indicating the duration and repetition of the proton pulse and the UCN intensity observed at a beamport.

Below we give a detailed description of key components for UCN transport, i.e. items with surfaces in contact with UCN, which are also included in the simulation model.

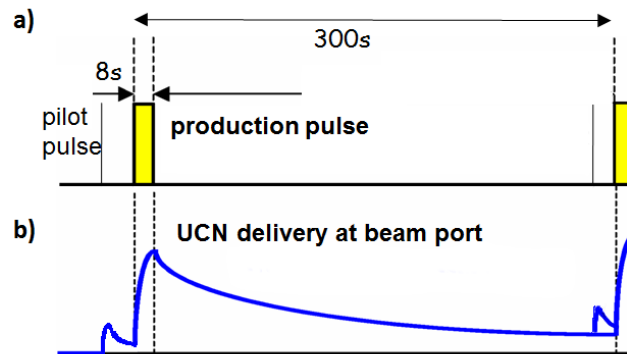


**Figure 3.** A typical pulse sequence during the operation of the UCN source. a) Sketch of the proton beam pulse timing towards the UCN spallation target. A 5 ms long pilot pulse is used to monitor beam centering and size. If approved, the main proton beam pulse with a maximum duration of 8 s is delivered 10 s later. A kick signal coincident with the pulse start triggers the flapper valve (No.4 in Fig. 1) closing sequence. The sequence can for example be every 300 s. b) Observed time distribution of UCN counts measured at the West-1 beamport.

## 2.1 D<sub>2</sub> vessel and lid

The D<sub>2</sub> moderator vessel is a sophisticated double-walled container with a volume of 44 l, engineered for cooling with super-critical helium at 4.9 K. A CAD image is shown in Fig. 4 together with a cut view. The cooling channels were wire-eroded into the bottom plate and the side walls (visible in the cut view) before all parts were welded together. A photo of the final vessel is shown in Fig. 5 .

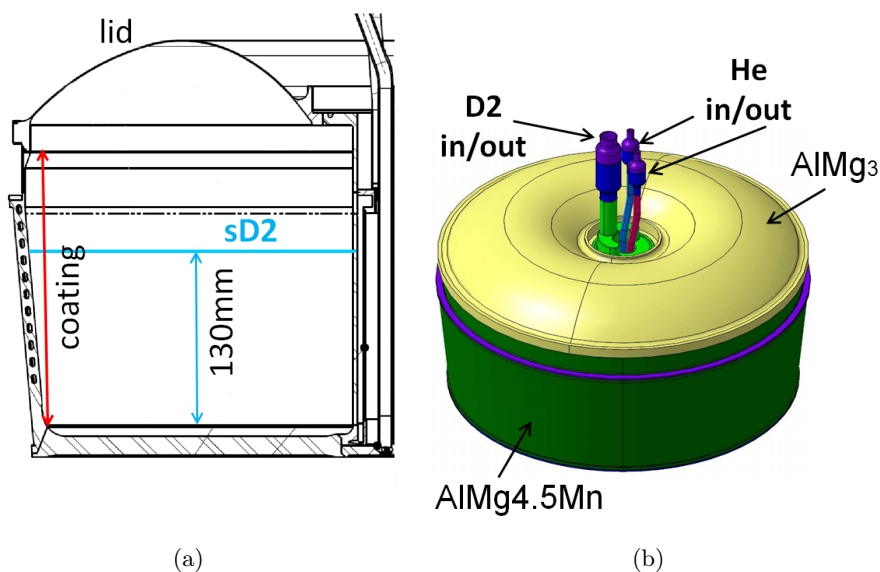


**Figure 4.** a) Cut view drawing of half of the moderator vessel with indicated height of coating and sD<sub>2</sub>. The dark circles on the outside wall indicate the cooling channels. b) CAD image of the moderator vessel. The D<sub>2</sub> filling tube is indicated. The two smaller tubes are used for supercritical He coolant in- and out-let.

Relevant for UCN transport is the coating on the inside of the vessel. The vessel with the exception of the top lid was galvanically coated with about  $70\ \mu\text{m}$  of nickel. In a second step, using sputter-coating<sup>1</sup>, a thin layer of about 400 nm of a nickel-molybdenum (NiMo) alloy with a 85/15 weight percent mixture was added on top.

The vessel lid with a thickness of 0.5 mm was machined from a single forged piece of AlMg3. A tolerance in thickness of less than  $\pm 50\ \mu\text{m}$  was maintained during production. This thin lid is necessary as the thickness of the material has a strong influence on UCN transmission [46]. In Fig. 5 the toroidally-shaped lid is clearly visible.

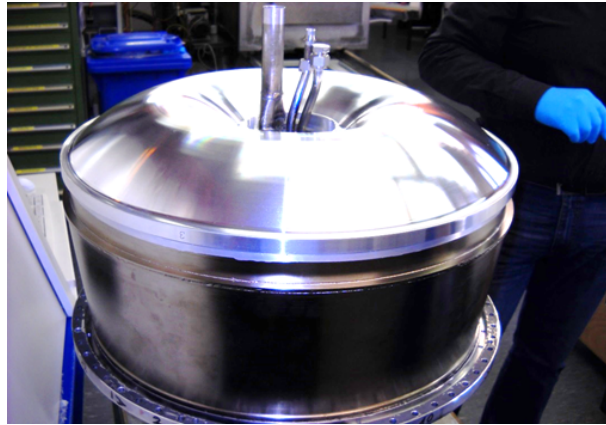


**Figure 5.** Photo of the sD<sub>2</sub> moderator vessel after assembly.

## 2.2 Vertical UCN guide

The vertical UCN guide is indicated as (3) in Fig. 1 and displayed in Fig. 6a. The sD<sub>2</sub> vessel is located inside, at the bottom of the vertical guide which serves also as a cryo-shield. During operation the vertical guide is cooled to about 80 K. This guide bridges about one meter of height between moderator lid and UCN storage vessel. This vertical rise decreases the UCN kinetic energies by roughly the same amount as they gain via the energy boost when exiting the sD<sub>2</sub>.

The guide cylinder is made from ultra-pure aluminum. Four 25 cm-thick cylindrical pieces of aluminum were diamond-lathed on the inside to a surface roughness better than 100 nm, then machined with wall thicknesses of 2, 4 and 6 mm, and then welded together. Finally, the inside was sputter-coated with 400 nm of nickel-molybdenum. The surface roughness of the diamond-lathed surface was determined using atomic force microscopy (AFM). The scan of one cylindrical piece is shown in Fig. 7. The grooves from lathe machining are visible with a groove depth of about  $\pm 100\ \text{nm}$ , which can be determined in the profile view.

<sup>1</sup> S-DH GmbH Heidelberg Hans-Bunte-Str.8-10, 69123 Heidelberg, Germany, <http://www.s-dh.de>

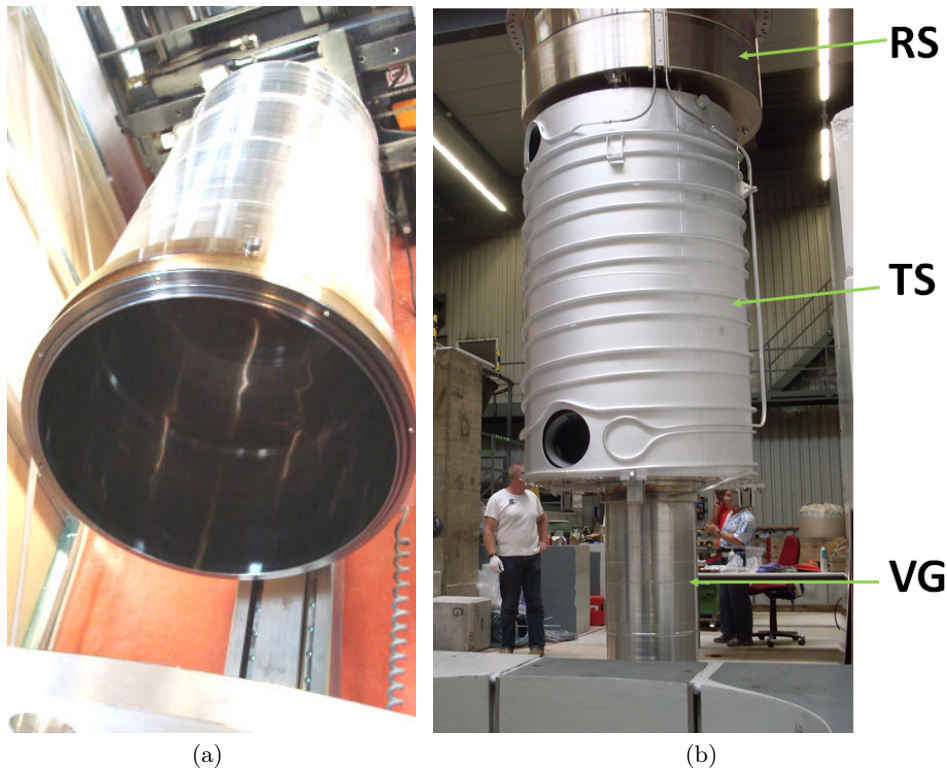


**Figure 6.** a) View of the vertical guide after coating with a highly reflective surface inside.  
 b) Final assembly with vertical guide (VG) on the bottom, thermal shield (TS) for the storage vessel, and stainless-steel radiation shield (RS). The two visible big openings are for the UCN ports, South (bottom) and West-2 (top).

### 2.3 UCN storage vessel

The UCN storage vessel, indicated as (SV) in Fig. 2 has a volume of about  $1.58 \text{ m}^3$  and an inside surface of  $95'500 \text{ cm}^2$ . During operation it is cooled to around 80 K. It is made from machined aluminum plates which were joined carefully together to prevent gaps between the plates as well as shape modification of the assembled vessel during cool down. Depending on the size such gaps can cause large UCN losses. The total area of gaps of the assembled storage vessel was therefore minimized. A rough mechanical measurement at room temperature resulted in a gap fraction of about  $5 \times 10^{-4}$  of the total surface. Two photos of the storage vessel are shown in Fig. 8.

The inside surfaces of the storage vessel open to UCN are all machined to a roughness of about 400 nm. The plates were galvanically coated with nickel (thickness about  $60 \mu\text{m}$ ) and finally coated with diamond-like carbon (DLC)<sup>2</sup> which was found to have excellent UCN storage properties [47–52]. The thickness of the DLC coating varied between 1 and  $2 \mu\text{m}$  depending on position during the coating process. The material optical potential of a sample plate coated

<sup>2</sup> Fraunhofer-Institut für Werkstoff- und Strahltechnik, Fraunhofer Projektgruppe at the Dortmunder Oberflächenzentrum, Eberhardstrasse 12, 44120 Dortmund, Germany, [www.iws.fraunhofer.de](http://www.iws.fraunhofer.de)

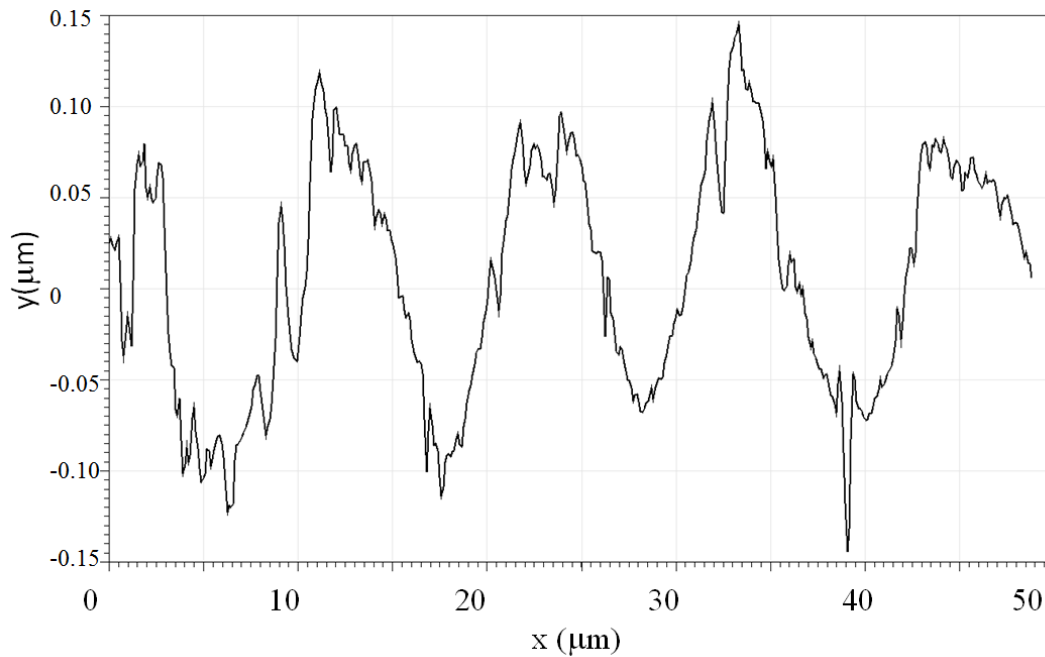


**Figure 7.** Profile view of an AFM scan before coating of the surface of the vertical guide over a length of  $50\mu\text{m}$  showing a groove depth of  $\pm 100\text{ nm}$ . Due to the softness of the pure aluminum the surface showed a typical structure coming from the diamond-lathe machining.

with DLC in the same process as the storage vessel plates was measured at a cold-neutron reflectometer [53]. A neutron optical potential between of  $235\pm 10\text{ neV}$  was determined.

The central tube inside the storage vessel serves as supply tube for cryogenic liquids to the moderator vessel and is shown in Fig. 9. It is made of Al and coated with DLC on the outside, identically as the vessel plates. The hole on the bottom of the vessel can be closed by a valve made of two semi-circular flaps with 57 cm diameter, indicated as (4) in Fig. 1. A photo of the flapper valve is shown in Fig. 9. Machined from AlMgSi, the flaps were also galvanically coated with nickel and subsequently coated with DLC.

Closing of the flapper valve is triggered by a signal synchronized with the proton beam kick and done with a pneumatic actuator using helium. The closing time is around two seconds. Opening of the flaps takes about 10 s because the high impedance of the long helium feeding line results in a slow pressure build-up in the actuator cylinder. The slow opening does not significantly influence the UCN performance. Timing between the flap-closing signal and the beam signal was optimized and shows a  $\pm 100\text{ ms}$  flat maximum as seen in Fig. 10 displaying the UCN count rate at beamport West-2 as function of the closing time of the flapper valve. In practice this is the time difference between the kick signal coincident with the rising flank of the proton beam pulse (see Fig.3) and the time when the flapper valve starts closing.



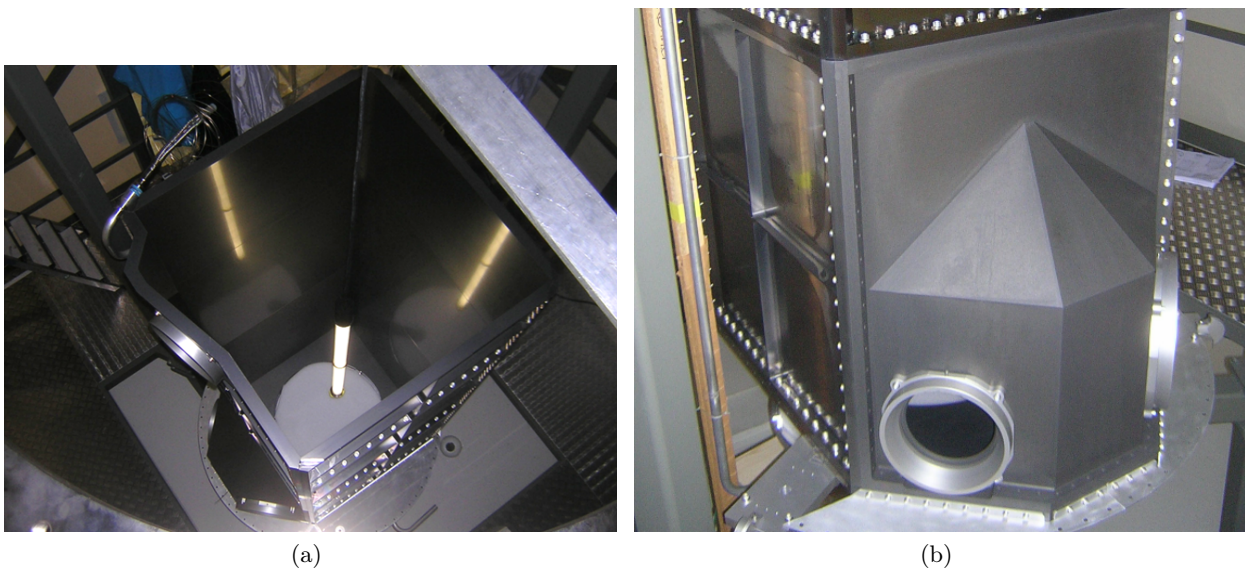


**Figure 8.** a) View inside the assembled UCN storage vessel from the top. On the left the exit for guide West-2 is visible. On the bottom the circular hole connecting to the vertical guide is visible. The reflection of the lamp demonstrates the surface smoothness and dark gray color of the diamond-like carbon coating. b) Outside of the guide exit section after coating. The large openings are the connection ports for the UCN guides, West-1 (left) and South (right).

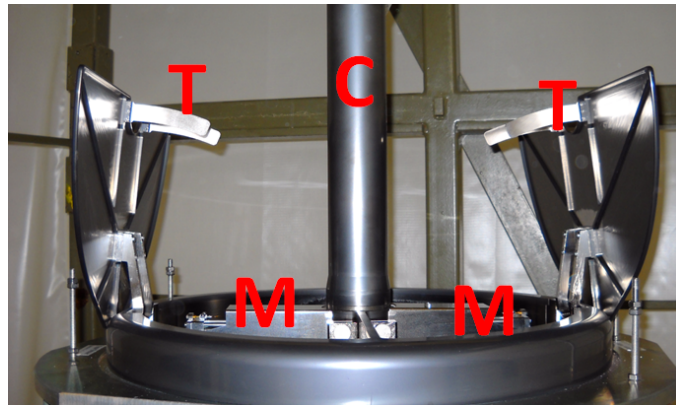


**Figure 9.** Photo of the open flapper valve in the test setup. The visible ‘teeth’ (T) are made from pure aluminum and serve in combination with magnets (M) as eddy-current brakes to smoothen the flap closing. (C) indicates the central tube.

## 2.4 UCN guides

Three UCN guides connect the storage vessel to the beamports in the experimental areas, see Fig. 2. The guide quality, mainly defined by low surface roughness and uniform coating with suited materials, is of paramount importance in order to minimize UCN losses on the long path to experiments. The length of the individual guide sections to the beamport West-1 is 7.090 m, to West-2 is 8.618 m, and to South is 7.049 m. The diameter was optimized by MC simulations to find a compromise between better transmission (large diameter) and less UCN density dilution (small diameter).

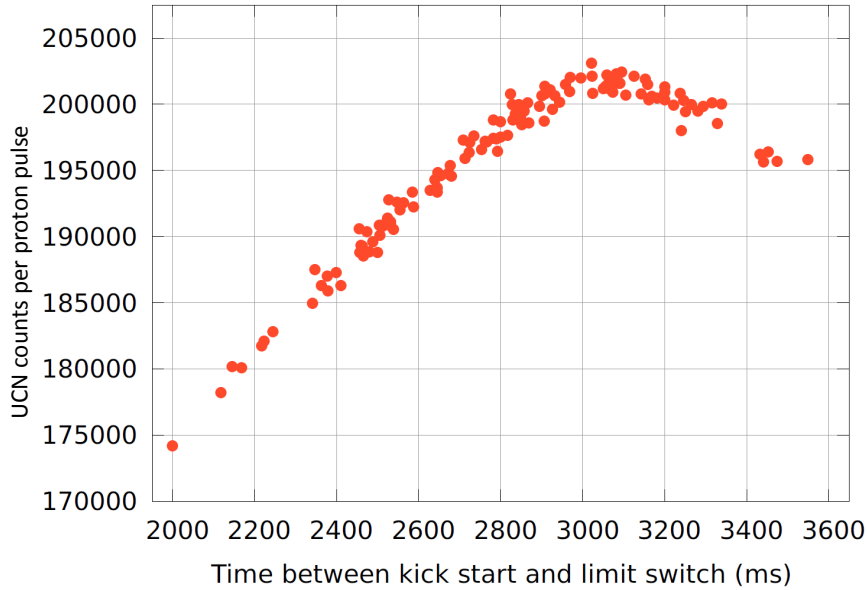


**Figure 10.** Correlation plot of the measured UCN counts at the West-2 beam port and the measured time difference between the kick signal and the time when the first flap of the flapper valve starts closing. For the measurement, the delay of the command to close the flapper valves has been varied. The intensity maximum is selected to be the optimized closing time.

The straight guide sections were made from Duran<sup>TM</sup> glass tubes<sup>3</sup> with a surface roughness better than 1 nm and therefore an expected high UCN transmission [54]. The inside diameter of the tube is 180 mm, the wall thickness is 5 mm.

Two sections per guide were made from stainless steel: 1) A bent was necessary for radiation protection to prevent a direct line of sight between experimental area and storage vessel. 2) Stainless steel was chosen as it increases the radiation hardness of the first meter guide docking directly onto the storage vessel and containing the neutron guide shutter.

All metal tubes were honed on the inside and then hand-polished to a surface roughness below 10 nm. All surfaces exposed to UCN were characterized using atomic-force microscopy as shown for a typical glass surface in Fig. 11. The profile view shows a smoothness for a glass tube to be below 2 nm.

All guide parts were either glued together, (the radiation hardness of the glue was tested, see [55]), or screwed tightly together, in order to minimize gaps, which could cause significant UCN losses. Figure 12 shows a photo of one metal guide. Figure 13 shows a picture of a finished glass guide. Figure 14 shows a photo of the end section of a glass guide during the production process. The end section was ground and smoothed over the entire diameter

<sup>3</sup> SCHOTT AG, Hattenbergstr. 10, 55122 Mainz, Germany

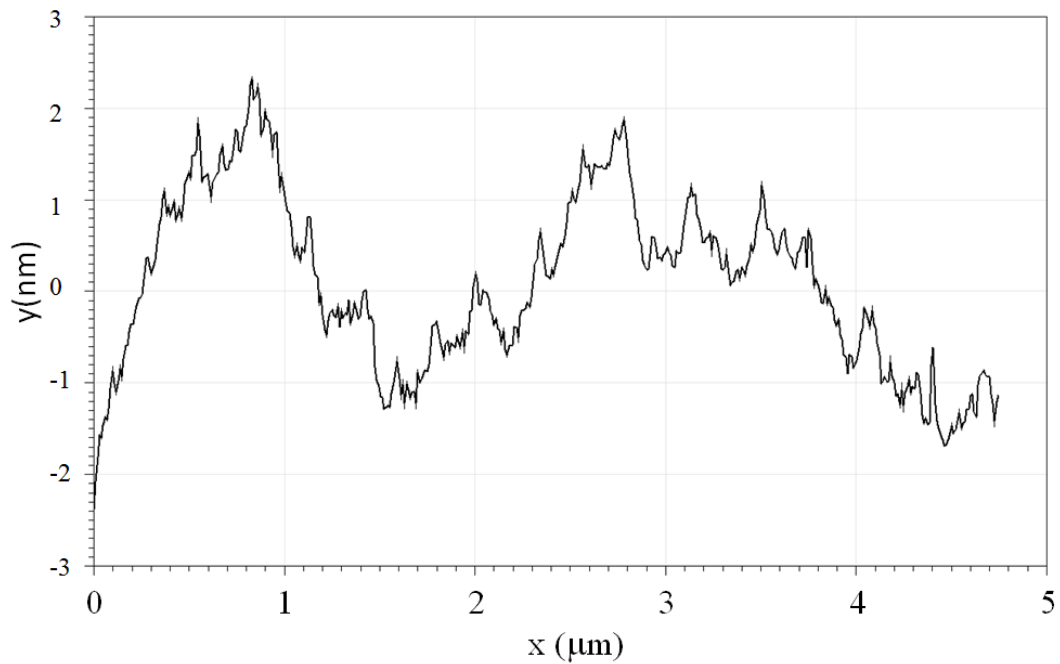


**Figure 11.** Display of an AFM measurement of the smooth glass surface inside a UCN guide over an area of  $5 \mu\text{m}$  side-length.

to guarantee the dimensions and then flame-polished to prevent chipping. A stainless steel end-ring was glued onto the prepared glass guide providing good protection of the glass and minimizing gaps. Any left-over small gap was filled with glue [55] and then sputter-coated with the entire guide in one process. The stainless steel guide attached to the storage vessel serves also as thermal insulator between the storage vessel at 80 K and the glass guide at room temperature. It contains the neutron guide shutter at its front end shown in Fig. 15.

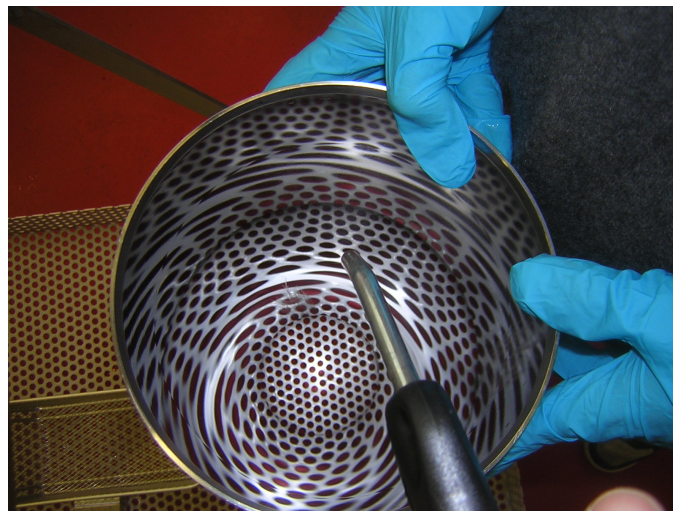


**Figure 12.** Photo of a stainless-steel guide during cleaning. The optical reflection is an indication of the high surface quality.

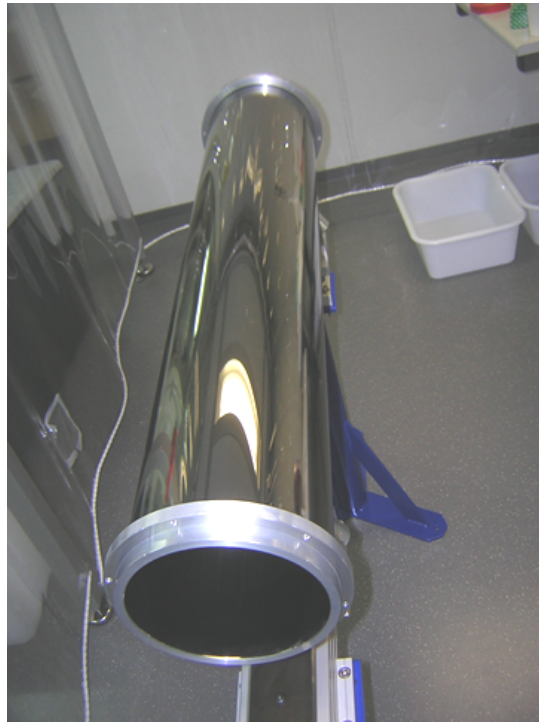


**Figure 13.** Assembled UCN glass guide.

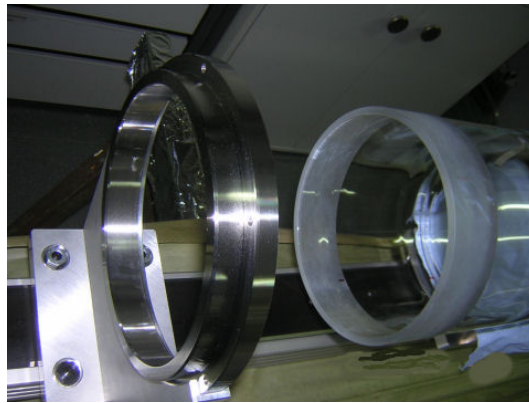


**Figure 14.** UCN glass guide end section before gluing the metal end-cap. The end of the glass tube was carefully ground and then flame-polished to fit well the metal end-cap in order to minimize gaps. The reflections show the high surface finish.

All surfaces exposed to UCN during operation were finally sputter-coated with nickel-molybdenum (NiMo) with a weight ratio of 85% to 15%. Additional small flat glass pieces were attached to the tubes during the coating process to allow cold-neutron reflectometry afterwards. Measurements of all guide samples at the NARZISS reflectometer [53] resulted in a material optical potential of  $220 \pm 10$  neV. One result of such a measurement of a NiMo coating is shown in Fig. 16.



**Figure 15.** Photo of the DLC-coated neutron guide shutter South in open position from the inside of the storage vessel. The visible four small openings on the bottom of the tube served to position the endoscopic UCN counters of Ref. [56].

The guide shutters and tubes indicated as No. (6) in Fig. 1, and shown in Fig. 15 for guide South, are part of the storage vessel and therefore coated with DLC. Opening and closing times of the guide shutters were measured to be below 200 ms.

The UCN transmission of all installed guides was measured prior to installation and found to be about 98% per meter for all glass and stainless-steel tubes [22].

#### 2.4.1 Minimizing gaps:

Gaps along the UCN transport path can cause large losses, therefore we tried to minimize gaps in the design and construction of the entire UCN path. All metal flanges were precisely machined and glued onto the glass guides as shown in Fig. 14. The metal guides and glass guides were then firmly connected by screws. The front section, where the guide connects to the storage vessel was pushed inside a concave receptacle on the storage vessel plate. Strong mechanical springs were mounted to keep the tension to this guide section towards the storage vessel in order to stay firmly connected when the storage vessel is cooled to about 80 K. Otherwise, gaps with the size of the order of millimeters could open due to thermal shrinking. The bend section of guide West-1, Fig. 17, shows the connections between metal guides and glass guides, and also the four springs pushing the guides towards the storage vessel. After installation the gap between guide end and window grid at the beamport was measured to be 0.3 mm (West-1), 5 mm (South), 0.1 mm (West-2) at room-temperature.

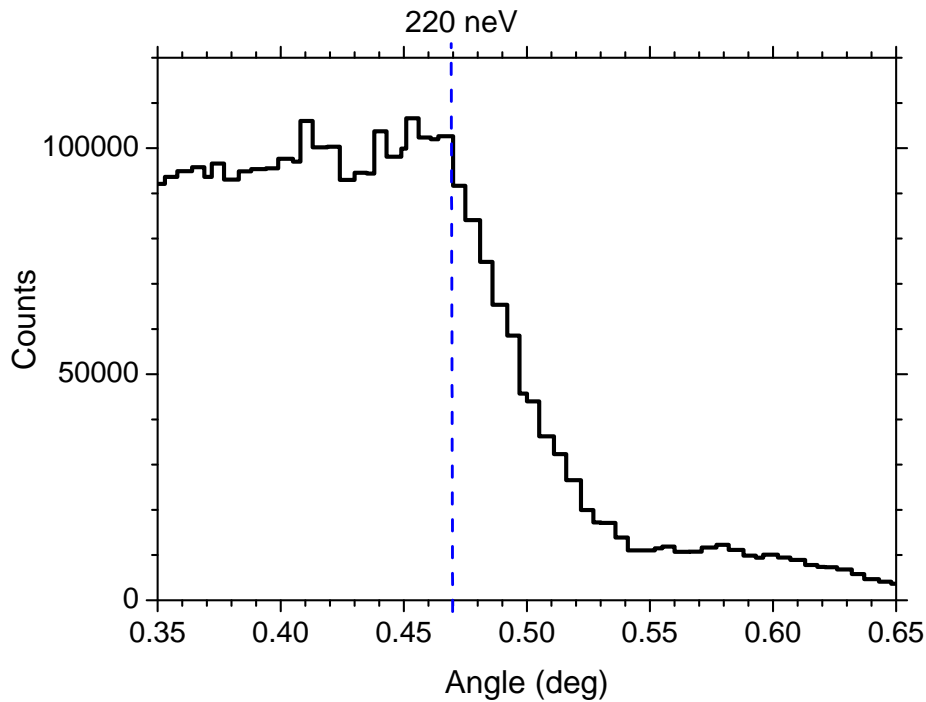


**Figure 16.** Plot of a cold neutron reflectometry measurement of one NiMo coating sample showing reflected neutron counts versus reflection angle. The vertical line indicates the angle corresponding to a neutron optical potential of 220 neV.

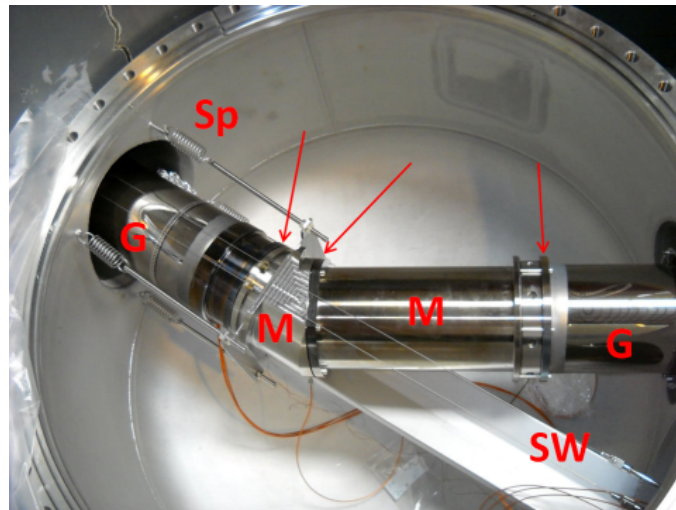


**Figure 17.** Photo of the bend section showing the connections (indicated with an arrow) between metal guides (M) and glass guides (G). The springs (Sp) pushing the front guide towards the storage vessel are visible. The two stainless steel wires (SW) on top of the guide are used to mechanically open and close the neutron guide shutter. The optical cable serves as readout for a monitoring detector [56].

## 2.5 Safety window

The safety windows at the end of the UCN guides separate the UCN source vacuum from the experiment vacua.

Figure 18 shows all parts of the window assembly which were finally welded together to assure vacuum tightness. It is

an important safety component and has therefore to withstand 3 bar overpressure from inside and 1 bar from outside. After a long performance test series [46], AlMg3 with a thickness of 0.1 mm was selected as window material because of its mechanical strength and good UCN transmission. Measurements of UCN transmission in the AlMg3 foil are reported in Section 4.4 below.

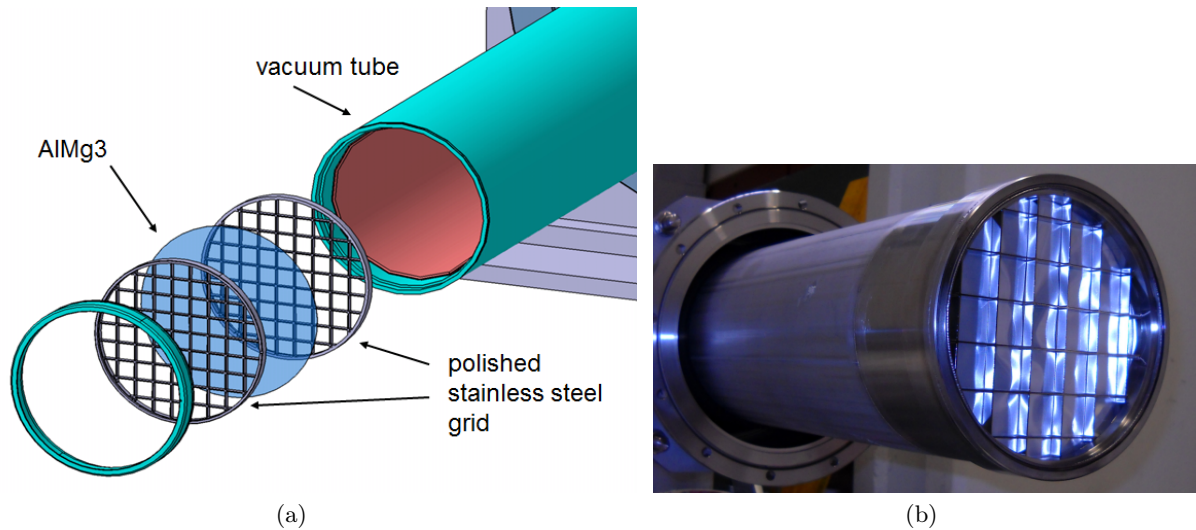


**Figure 18.** a) Expanded CAD image of the safety window section which separates UCN source vacuum from experiment vacuum. Shown are the two reinforcement grids, the AlMg3 foil, the vacuum tube and holding ring. All the shown parts were finally electron-beam welded for tightness. b) Photo of the installed safety window at the end of the vacuum tube of guide West-1.

All three guides accommodate a safety window located close to the beamport. On guide West-2 the expected average UCN energy spectrum is significantly softer due to gravitational shift, as the extraction is at a height of 2.3 m above the bottom of the storage vessel. Therefore an additional vertical section on guide West-2, shown in Fig. 19, was added. This causes the UCN to fall by one meter and increases the kinetic energy by 100 neV, well above the neutron optical potential of the AlMg3 safety window (54 neV).

The beamports West-1 and South were prepared for the installation of superconducting (SC) polarizer magnets. The safety windows would be located at the highest magnetic field of an installed SC magnet. The polarized UCN would have the highest velocities when passing the foil. For the nEDM experiment, beamport South was equipped with a magnet providing a 5 T field. UCN intensity measurements for various magnetic field strengths are described in Section 4.5 below.

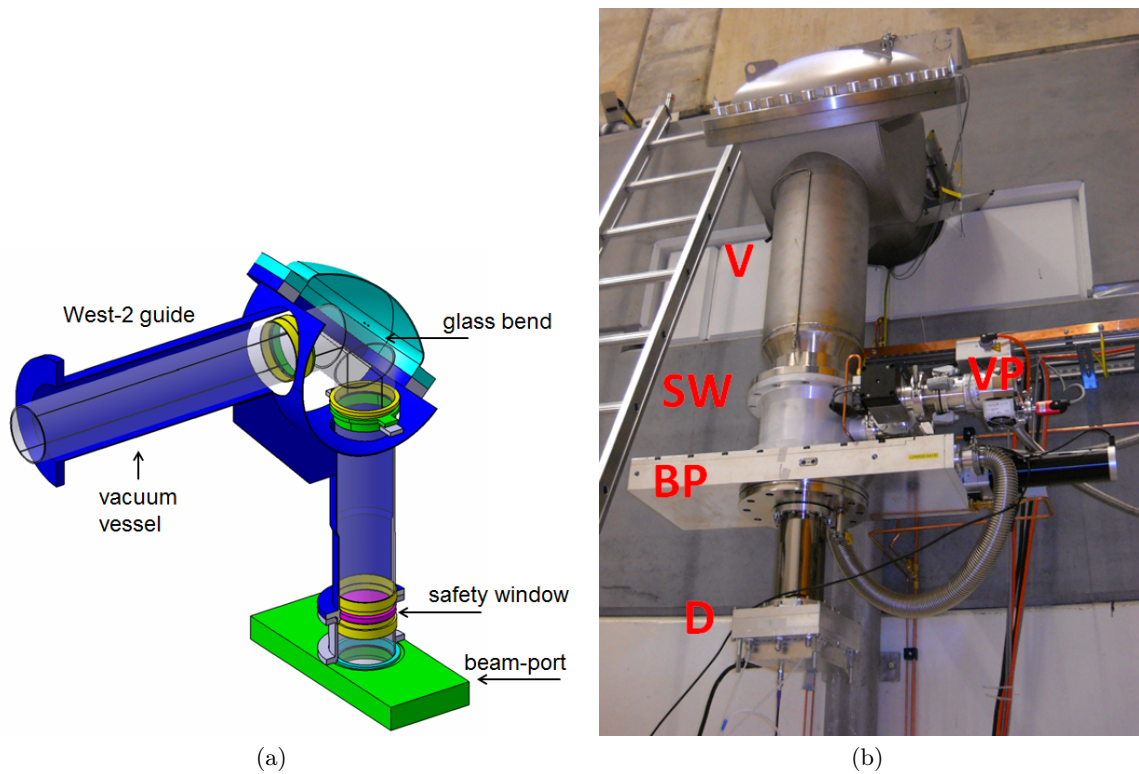


**Figure 19.** a) CAD image of the vertical bend section of the West-2 guide b) West-2 guide outside the biological shield with positions indicated for: vertical section (V), safety window (SW), beamport shutter (BP), small Cascade detector (D), vacuum pumps (VP).

## 2.6 Beamport shutter

Three large (DN200) vacuum shutters custom designed and produced by VAT<sup>4</sup> are mounted as beamport shutters indicated as BP in Fig. 19. All parts of the shutter exposed to UCN were coated with DLC. In Ref. [22] we have already reported on the properties of this shutter. Figures 4 to 6 of this reference depicted the measured opening area and opening function relevant for UCN transport modeling. The opening and closing times were measured to be about 1 s.

<sup>4</sup> VAT Group AG, Seelistr. 1, CH-9469 Haag, Switzerland



### 3 Simulation model for the PSI UCN optics

In order to relate the parameters and the geometry of individual parts of the UCN source and guides system to its overall performance, detailed Monte Carlo simulations were performed. A large number of alternative geometry configurations for the UCN optics system were simulated showing that the as-built configuration is optimal in terms of UCN yield. The general features of the PSI-developed simulation code, MCUCN, for ultracold neutron transport are summarized in Ref. [25]. This code was also used during the development of the UCN source at PSI to optimize the distance between the sD<sub>2</sub> vessel and the bottom of the storage vessel. Also the size and shape of the storage vessel, and the guide diameters were investigated, to provide preliminary predictions on UCN density and energy distribution.

#### 3.1 Geometry model of the PSI UCN source

In the geometrical model for MC simulations of the PSI UCN source we implemented (i) all surfaces coated with materials with high optical potentials (DLC, Ni, NiMo 85/15), and (ii) all gaps between guide sections which were approximated either as totally absorbing or having low material optical potential, e.g. aluminum. As basis for the input geometry we used technical drawings. The actual length of the neutron guides from storage vessel to beamport is implemented with an accuracy of 2 mm. The geometry starts with the lid of the solid deuterium vessel as shown in Fig. 4. However, instead of a half toroidal shape we implemented a dome. The latter definition was more straightforward and less run-time demanding than building a toroidal surface from a series of cone sections. Our previous MC comparisons of a dome and a toroidal shape gave the same results for the transmission of UCN because the average angular distributions of the surface normal are in both cases similar.

This lid constitutes the lower boundary of the vertical guide which directs the neutrons into the large storage vessel of the UCN source (see Figs. 8 and 1). This vessel has four flat sides. In the bottom part the two neutron guide exits are located in a niche. Important are also the time dependent position of the flaps separating the storage vessel from the vertical guide, as shown in Fig. 9. The neutron guide shutter at the storage vessel is shown for guide South in Fig. 15. Apart from the lid of the sD<sub>2</sub> vessel, we also included the vacuum separation foils, made from AlMg<sub>3</sub>, at the end of the UCN guides as introduced in Sec. 2.5. On guide South the foil was placed in the center of a 5 Tesla superconducting magnet which acts as UCN polarizer. Each virtual detector counts UCN through another, similar 100  $\mu$ m thick separation foil. The sensitive detector area is matched to the detector used in the actual measurement. For test calculations different experimental volumes were attached depending on the aim of the calculation.

In Figs. 20 and 21 the geometry of the UCN source part as appearing in the MCUCN model is visualized. The blue dots are points of reflection of UCN on their way to the beamports and example trajectories are shown in red. Such plots serve as first tests of the geometry and physics implementations.

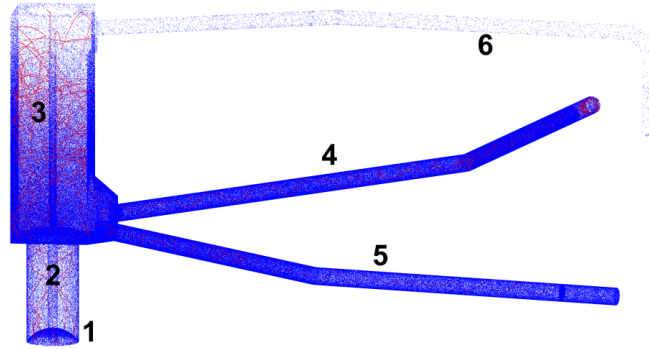


**Figure 20.** Simulation model of the UCN source visualized by example trajectories (red) and reflection points of UCN (blue) on the relevant neutron optics surfaces: 1 - lid separating the UCN source vessel from the vertical neutron guide, 2 - vertical neutron guide, 3 - UCN storage vessel, 4 - UCN guide South, 5 - UCN guide West-1, 6 - UCN guide West-2. The density of the reflection points is proportional to the number of wall interactions. Thus such 3D geometry visualizations serve at the same time as first visual tests of the physics implementation.

### 3.2 Coating parameters

We introduced three global coating parameters for the neutron guides between the storage vessel and the beamports:

1. an optical potential with a value obtained from cold neutron reflectometry measurements [48-50];
2. a loss parameter  $\eta$ , calculated from the ratio of the complex and real parts of the optical potential - independent of kinetic energy in agreement with experimental results [50,57];
3. a parameter  $p_{diff}$  for the fraction of diffuse reflections according to the Lambert model which is also independent of kinetic energy.

The history of the trajectories in the MC simulations show that the majority of UCN exiting the beamports have sampled the whole volume of the UCN source and the beamline and therefore we use such global i.e. spatially averaged parameters (the spacial averaging is of course not independent from the geometry configuration). Similarly, different values of the three global parameters were defined for the entire storage vessel of the UCN source, including shutters, and separately for the vertical guide between UCN converter and storage vessel of the source.

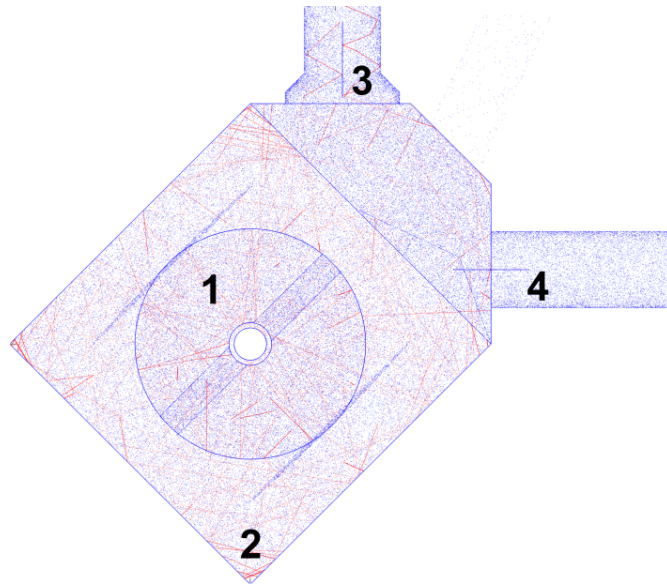


**Figure 21.** View from the top of the simulated geometry visualized by example trajectories (red) and reflection points of UCN (blue) depicting details of the storage vessel: 1 - top of the vertical guide (large circle) , 2 - storage vessel, 3 - neutron guide “South”, 4 - neutron guide “West-2”. The reflection points on the main flapper valves are plotted for both the closed state (within large circle) and the opened state (two narrow ‘clouds’ tangent to the large circle).

### 3.3 Initial trajectory parameters from the source

At the beginning of the simulation UCNs are generated with random initial coordinates (position, velocity and time) as described below according to probability distributions detailed in [1].

For the energy distribution of the UCN emerging from the solid deuterium surface, we rely on a linear approximation, i.e. on the initial linear section of a Maxwell flux (eq.(3.9) in [1]) for a high-quality, realistic  $sD_2$  converter. This assumption was strengthened by separate MC simulations of the UCN extraction efficiency from bulk  $sD_2$  for a close-to-optimal  $sD_2$  structure. They are in agreement with experimental data [58]. These calculations included (i) super-thermal UCN production, (ii) temperature-dependent thermal up-scattering, (iii) up-scattering on para-deuterium, (iv) Porod scattering [59], (v) absorption on hydrogen contamination, and (vi) reflection or absorption on the coating material of the converter vessel. We did not implement an interface distribution of macroscopic cracks in the solid deuterium since these are unknown and can be different after every freezing procedure. Such cracks represent deuterium-vacuum interfaces which can reflect UCN and hence increase their dwell time within the material and thus also the loss probability. We also did not implement intensity reduction due to the observed frost formation [26]. Consequently, our estimate of the absolute UCN flux constituted an upper limit and is not subject of this paper.

The angular distribution of the emerging UCN was set as a linear dependence in cosine of the angle to the surface normal. This is typical for moderators and for perfectly diffuse emitter models. On top of this angular distribution we added a vertical boost which corresponds to the optical potential of the  $sD_2$  [45]. Since we don't expect a perfectly

smooth deuterium surface for a real converter material we also modeled cases when this boost was not vertical but diffuse. In this case we kept the initial angular distribution mentioned above and only increased the total energy by 102.5 neV. Then the vertical transmission through the lid decreased by about 30%.

The initial position coordinates are generated according to a flat horizontal homogeneous distribution confirmed by our separate MC results on extraction from the sD2 into vacuum. Deviations from this distribution don't show a relevant influence.

## 4 Characterization measurements

A series of measurements were performed to characterize the UCN source components. Measurements were performed with UCN counters attached to beamport West-1 and West-2. Beamport South was used for a few measurements only as it permanently hosted the nEDM experiment [5, 7, 60] up to 2017 and has the n2EDM experiment [61] now being set up.

We used position-sensitive Cascade UCN counters<sup>5</sup> with active areas of 10 cm × 10 cm (referred to later as 'small') or 20 cm × 20 cm ('big'), the latter covering the full 180 mm diameter of the beam guide. UCN detection works via neutron capture on <sup>10</sup>B which is followed by emission of an  $\alpha$  particle and a <sup>7</sup>Li nucleus [62]. The detector entrance window, a 0.1 mm thick AlMg3 or Al foil is coated on the backside with a <sup>10</sup>B layer of 200 nm. The UCN transmission in the Al part of this entrance window is about 0.7 [63].

In standard operation, UCN counts are monitored with the big cascade detector mounted on beamport West-1 and one small cascade detector mounted on beamport West-2.

### 4.1 UCN counts time distributions

The time distribution of UCN counts arriving at a given beamport reflects the emptying time of the storage vessel and UCN guide through the defined opening of the neutron guide towards a detector. The time behavior can be described with an exponential function and a characteristic time constant ( $\tau$ ) which for storage measurements is called storage time constant (STC)

$$N(t) = I \times e^{-\frac{t}{\tau}} \quad (1)$$

---

<sup>5</sup> CDT CASCADE Detector Technologies GmbH, Hans-Bunte-Str. 8-10, D-69123 Heidelberg, Germany

We mainly worked with three configurations: Figure 22 shows the observed UCN counts over a full period of 300 s between proton pulses for three different operation modes, i.e. configurations of the UCN source.

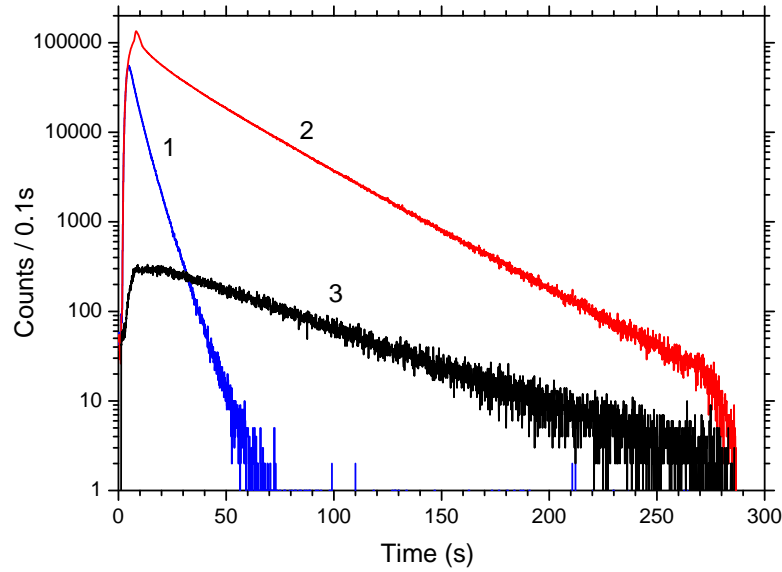
1) Benchmark pulse: A benchmark pulse is a 2 s long proton beam pulse with a box-shaped profile. All shutters are open and hence no mechanical movements influence UCN delivery. This mode is used in order to guarantee close to identical conditions for measurements distributed over many years. As the storage vessel flapper valve stays open, UCN are rapidly lost due to back-reflections through the large opening (a factor of 9 larger area than the guide exits) and subsequent absorption in the sD<sub>2</sub> solid.

2) Production pulse: In standard operation, i.e. providing production pulses, the UCN storage flapper valves close at the end of the proton pulse preventing further back-reflection towards the sD<sub>2</sub>. UCN are then emptied towards the beamport over the full period between subsequent pulses. The UCN count rate rapidly increases during the pulse. After the flapper valve is closed the rate decreases with the emptying rate of the storage vessel and guide system through one or in this example two guide openings, 254 cm<sup>2</sup> each. At 280 s the flapper valve opens again in preparation of the next beam pulse, therefore the remaining UCN are quickly lost.

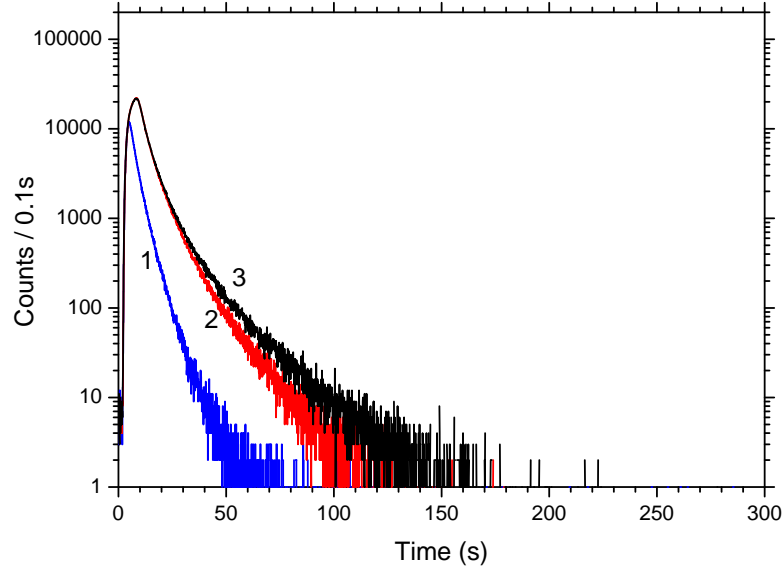
3) Leakage mode: In leakage mode the neutron guide shutter towards the beamport stays closed. The shutter is not perfectly tight and UCN can leak through and travel from the exit of the storage vessel to the detector. The initial emptying rate is smaller and has a longer time constant compared to case (2). This mode is used to determine the storage time constant of the storage vessel. At 280 s the flapper valve opens.

Figure 23 displays the same three cases as in Fig. 22, but at beamport West-2. The UCN intensity is about a factor of 10 smaller due to i) the extraction height of guide West-2 which is 2.3 m above the storage vessel floor and ii) using the small Cascade counter. After about 100 s all UCN with energies above 230 neV at the level of the West-2 storage-vessel exit are extracted or lost, and the UCN intensity is rapidly approaching zero. Also the observed storage time constants are smaller than at beamport West-1 as the observed UCN which can reach the West-2 beamport have on average higher energies at the bottom level and therefore are lost faster. The fact that neutron guide shutter West-1 is closed, influences the UCN intensity at West-2 only at very late times as can be seen by the higher intensity of curve 3) in comparison to curve 2).

Depending on the open or closed state of the main flapper valves of the storage vessel and the different neutron guide shutters the storage time constants differ. The resulting characteristic time constants from fits of Eqn.4.1 to the data are listed in Tab. 1.



**Figure 22.** UCN counts observed at beamport West-1 for three different operation modes: 1) benchmark pulse ( $\tau = 5.0$  s); 2) production pulse ( $\tau = 36.0$  s); 3) leakage operation with neutron guide shutter closed ( $\tau = 90$  s). The bin width is 100 ms, values from Tab.1.



**Figure 23.** Same as Fig. 22 but observed at beamport West-2. Bin width is 100 ms.

## 4.2 UCN intensity development

In order to characterize the intensity of the UCN source and compare it over long time periods we have used benchmark pulses and production pulses. Benchmark pulses do not involve any mechanical movements and should therefore track

Source Configuration	$\tau$ [s]
SV-Flaps closed	
West-1 open	$36.1 \pm 0.2$
W-1 & South open	$31.6 \pm 0.7$
SV-Flaps open	
2 flaps open	$5.0 \pm 0.4$
one flap closed	$6.9 \pm 0.2$

**Table 1.** List of storage time constants measured with a detector on beamport West-1 and with different shutter configurations (see also [23]). The shutter to West-2 was always open and does not significantly influence the time constants.

the status of the UCN production and extraction in the sD<sub>2</sub>, under the assumption of no changes in UCN transport through storage vessel, guides and windows. The observed intensity increase over the years, shown in Fig. 24, tracks the improvements in preparation and modification of the sD<sub>2</sub> and the increased duty cycle. In Fig. 25 the largest UCN yield measured from production pulses on beamport West-1 is shown for each year. Actual measurements took place at proton beam currents of 1.8, 2.2, 2.4 mA and were normalized to 2.2 mA for the plot. Both plots show a dip in 2014 because a different experimental setup was online [57] when the UCN source actually performed best, hence no standardized characterization measurement was taken at the best source conditions.

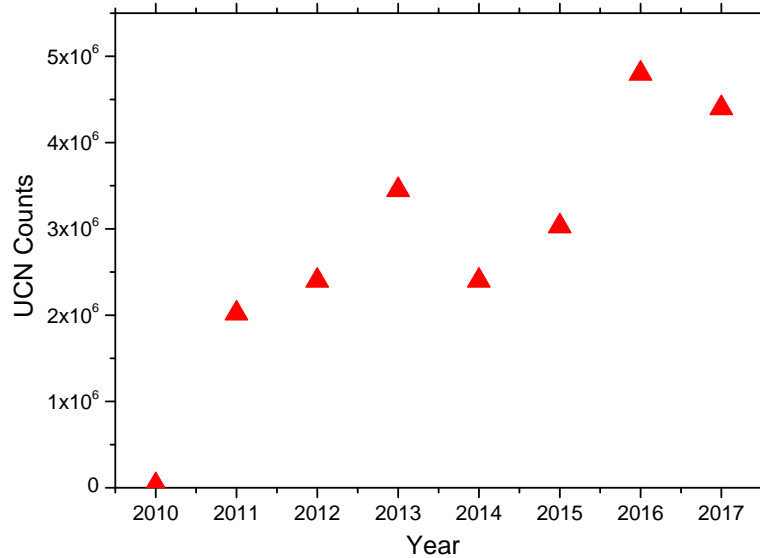


**Figure 24.** Highest UCN output for a benchmark pulse observed on beamport West-1 in a given year, normalized to the proton beam current of 2.2 mA.

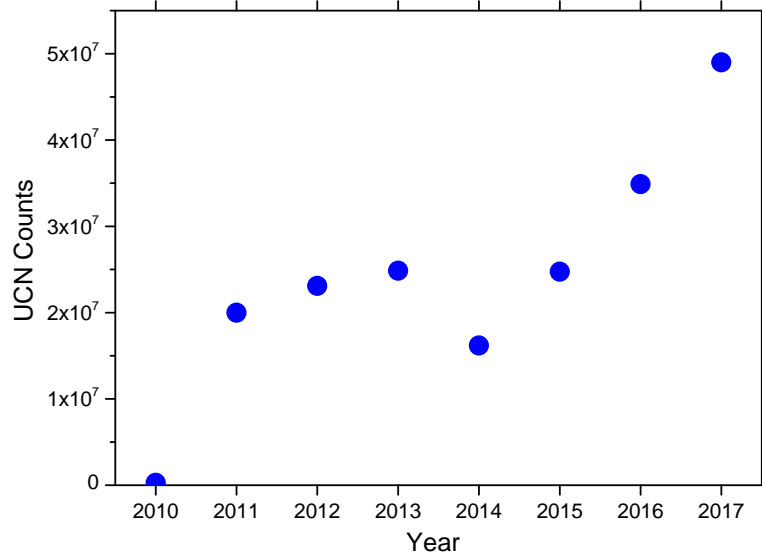


**Figure 25.** Highest UCN output for a production pulse observed on beamport West-1 in a given year, normalized to the proton beam current of 2.2 mA.

### 4.3 Storage time constants of the UCN storage vessel

The storage time constant of the storage vessel can be determined in two ways. The 'classical' method [1] proceeds in three steps:

1. filling the storage vessel with UCN;
2. closing all UCN shutters and storing the UCN for a given time;
3. opening the shutter towards the detector and counting all surviving UCN.

The leakage method as described in Sec. 4.3.2 is an alternative way to measure the decrease of the UCN density in the storage vessel. With both methods the time dependence of the observed UCN intensity can be fitted with a single (or double, or multiple) exponential function with the slope defining the storage time constant(s) (STC).

#### 4.3.1 Classical method

Measurements using the classical method were performed with a Cascade counter mounted on beamport West-1. We have measured the number of UCN in the vessel as a function of time for storage times between 5 and 350 s. By choosing different fit regions one can obtain information about the behavior of the storage vessel with respect to the UCN velocity spectrum. A fit to the entire data-set yields a  $STC = 94.5 \pm 0.9$  s for a single exponential as shown in



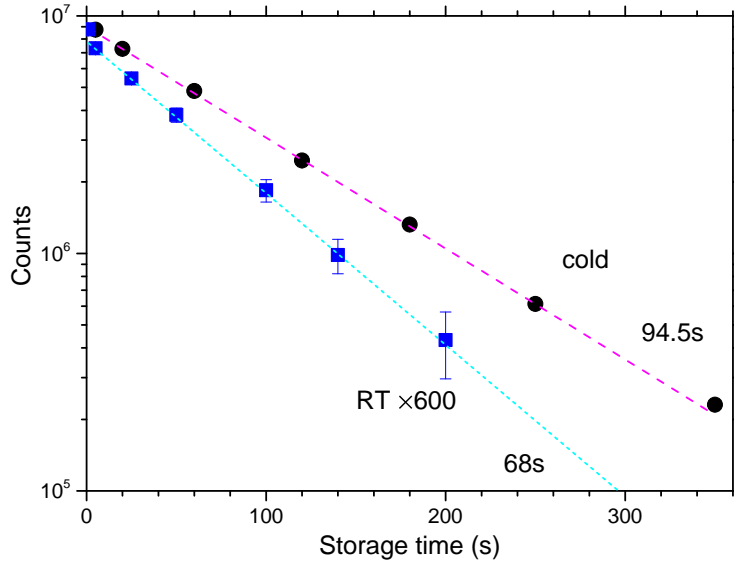


**Figure 26.** UCN counts observed after a given storage time in the storage vessel: a) at operating conditions around 80 K in 2011. The dashed line guides the eye with a single exponential decay function and a storage time constant of 94.5 s. b) at room temperature with gaseous D<sub>2</sub> for UCN production. The dotted line shows a fit with STC=68 s.

Fit range (s)	STC (s)
5 - 300	94.5±0.9
5 - 20	80.0±10.0
180 - 350	97.2±0.5

**Table 2.** Storage time constants from single exponential fits to the storage measurement at cold operating conditions in 2011. (see also [23]).

Fig.26. In principle every UCN energy group has a separate storage time constant. It is common to define two groups which are discernible with separate storage time constants. The short time range is dominated by the influence of spectral cleaning which takes some time until UCN with kinetic energies above the optical potential of the walls are lost. But it also characterizes the group of faster UCN. Since these interact more often with the wall materials they are lost faster. After longer times only slower UCN survive resulting in a larger STC. Table 2 lists the result obtained for different fit ranges.

In order to understand the temperature dependence of losses due to thermal up-scattering, we also performed a measurement with the storage vessel at room temperature. This could only be done with very low UCN statistics and in a non-standard operation mode where the entire UCN source was at room temperature. The UCN intensity was therefore very low, as the UCN production took place in gaseous D<sub>2</sub> at room-temperature and 1 bar pressure, hence under very disfavoring conditions. The results are plotted in Fig. 26. A STC of 68 s was determined, with the at 2 s measurement outside the fit range.

Year	STC (s)
2011	89±1
2012	84±1
2013	79±1
2014	83±1
2017	83±1
2018	85±1

**Table 3.** Storage time constants from exponential fit to the storage measurement at cold operating conditions in different years since start-up. Data were binned to 1 s and a fit in the range of 40 to 220 s after proton pulse start [24].

#### 4.3.2 Leakage method

The ‘leakage method’ makes use of the fact that the neutron guide shutters are not perfectly UCN tight but cause a small UCN leakage on the order of 1%. The intensity of these leaking UCN decreases exponentially with time described with the STC of the UCN storage vessel. The measurement is shown in Fig. 22 by curve 3 which was fitted with a single exponential function. The results confirm the classical measurement.

Several measurements were conducted in subsequent years of operation which were separated by periods of warming up the entire facility to room temperature, and venting of the storage vessel and guides. Furthermore, some maintenance work was typically performed during such shutdown periods. The measured STCs with a single exponential fit in an identical fit range, given in Tab. 3, agree within a small range of a few seconds. The lower values observed in 2013 could not be conclusively explained. The small changes could be due to variations in closing of the flapper valve of the storage vessel, in closing of the neutron guide shutters, or to the UCN energy spectrum from changing conditions of the sD<sub>2</sub> bulk and surface. A change in vacuum conditions, i.e. rest gas, is excluded.

#### 4.4 Transmission through AlMg3

UCN have to penetrate solid AlMg3 material on their path from production to detection at two positions which are required by hydrogen safety regulations:

- 1) the lid of the solid deuterium moderator vessel (thickness = 500 μm) (see Fig. 4);
- 2) the UCN vacuum window at the end of the UCN guides (thickness = 100 μm) (see Fig. 18).

It was previously shown that measured transmission through Al foils cannot be correctly calculated by relying only on the Al absorption cross-sections and material densities which consistently overestimates the transmission [46]. Therefore we have pursued several investigations into the UCN transmission properties of the AlMg3 material used in the foils.

Measurements were performed using a Cascade detector mounted after a foil holder in the UCN path. Different foils with 70 mm diameter were inserted. The setup was installed on beamports West-1 and West-2. The two positions allowed to see the influence of different UCN energy spectra on the transmission.

1) Production pulse on West-2: The West-2 port extracts UCN from the top of the storage vessel at 230 cm height. After a 1.3 m vertical section before the beamport (see Fig. 19) all UCN have a minimum energy of  $\sim 130$  neV due to gravitational acceleration. Two 90-degree UCN guide bends made from stainless steel after the vertical section were used to cut off the UCN with kinetic energies above the stainless steel neutron optical potential  $\sim 190$  neV.

2) Production pulse on West-1: At this port UCN energies start at 50 neV (passing the safety foil) and are well populated up to the guide coating material optical potential of 220 neV.

A fraction of higher energy neutrons is also present as shown in MCUCN simulations (see Fig. 43). In the following we discuss the two types of safety windows.

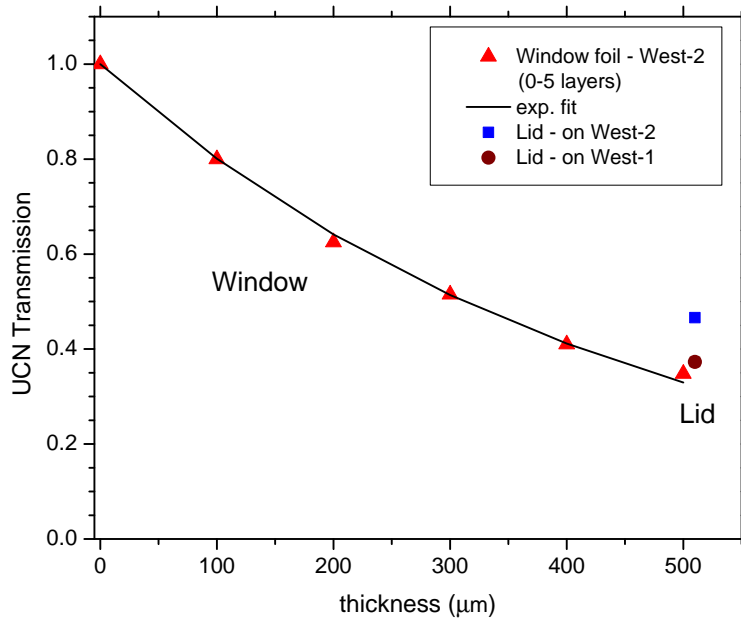


**Figure 27.** Measured UCN transmission for up to 5 layers of the window safety foil (filled triangles) and the moderator vessel lid (filled circle and square) at various beam conditions. The line represents a fit to the foil measurement taking into account the shape of the simulated energy spectrum in West-1. This fit yielded a factor of  $2.1 \pm 0.1$  multiplying the theoretical loss cross-section (see text Sec. 5).

#### 4.4.1 D<sub>2</sub> moderator vessel lid

The  $0.5 \pm 0.05$  mm thick material used in the lid measurement was machined in the same way and from the same bulk AlMg3 material as the installed moderator vessel lid. This was possible as the moderator vessel had an identical twin which passed a burst-pressure test demonstrating functionality up to 7 bar. After this burst test, large undamaged parts of the damaged lid could be re-used for UCN transmission measurements at the West-2 and West-1 beamports. The results are plotted in Fig. 27. It is obvious, that a lower UCN kinetic energy reduces the UCN transmission. We remind the reader that UCN gain about 100 neV in kinetic energy when exiting from the sD<sub>2</sub> due to its neutron optical potential [45]. Therefore, the UCN energies at the lid position starts at 100 neV. The height difference of the West-1 and West-2 beamports selects a different UCN energy spectrum. The measured values are consistent with one previously obtained using a similar Al-alloy [63] measured at the TRIGA Mainz UCN facility [64].

#### 4.4.2 Window foil

The material for the UCN transmission measurement of the window safety foil was taken from the same 0.1 mm thick AlMg3 foil roll as the original window foil used for the installed safety windows (see Sec. 2.5).

Measurements on West-2 were performed with a stack of up to five foils, demonstrating the expected exponential decrease with thickness displayed in Fig. 27. One can see that while having the same material thickness of 0.5 mm, five foils together have a smaller UCN transmission than a single 'thick' piece. This is probably due to additional reflections on the individual foil surfaces.

Calculating the UCN transmission from absorption cross-section values for known material compositions results typically in a large underestimation of the UCN transmission as already observed previously in [46]. Therefore experimental transmission values were used to tune the loss cross-sections in the Monte-Carlo simulation. It required increasing the theoretical cross-section by about a factor of factor of  $2.1 \pm 0.1$  consistent with the findings in Ref. [46]. These effective cross-sections can then reproduce the observed UCN transmission values. These were used in our simulation model of the PSI UCN source as outlined in Sec. 3.

### 4.5 Transmission measurements through the superconducting magnet

As described in Section 2.5, beamport South was equipped with a SC magnet. Because of the magnetic moment of the neutron interacting with the magnetic field ( $\pm 60$  neV/T) the UCN velocity of the transported UCN is affected in a magnetic field and therefore also when passing this AlMg3 window. We have performed transmission measurements for

various field values in order to further constrain the UCN energy spectrum from the source. The big Cascade detector was mounted directly at that beamport to investigate the window transmission as a function of magnetic field. No additional spin analysis system was used. With this setup the dependence of the UCN rate for various magnetic fields in the range of 0 T to 5 T, using production pulses with 3 s length and benchmark pulses with 2 s were measured.

#### 4.5.1 UCN intensities

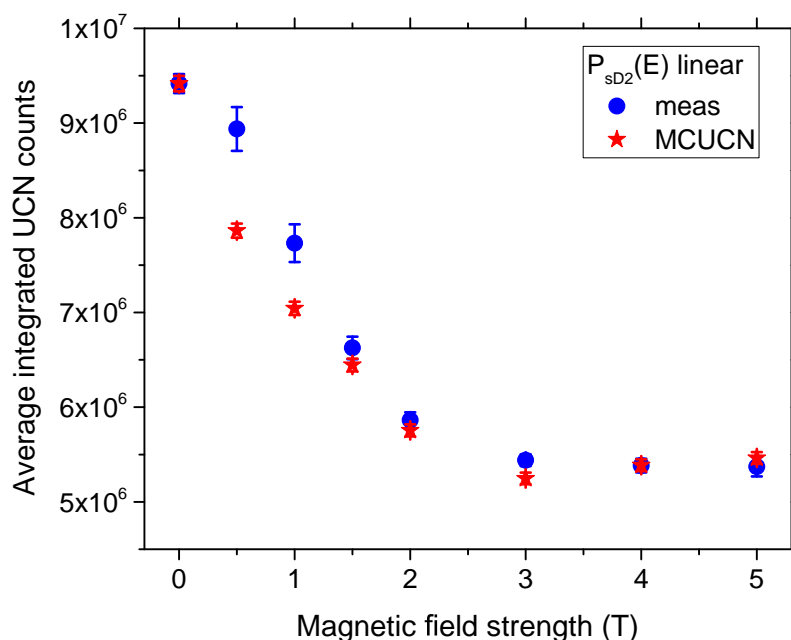


**Figure 28.** UCN counts for different SC magnet fields integrated from 1 s after the end of the proton beam kick up to 300 s. Measured values (filled circles) are averaged over 3 proton beam kicks. Filled stars mark the intensities resulting from the simulation, with a linear energy spectrum from the sD<sub>2</sub>. The difference at 0.5 and 1 T shows that the low energy range of the UCN spectrum is not yet well modeled as this is just above the AI threshold of the safety window.

Integrated UCN counts for the different magnetic fields, measured in 3 s production pulses are shown in Fig. 28. Table 4 lists the intensities, both, for benchmark pulses and production pulses. In order to exclude faster neutrons occurring during the proton pulse, the integration time started 1 s after the end of the pulse. With increasing magnetic field magnitude, lower rates of UCN were registered in the detector. This is expected, as half of the neutrons – i.e. one spin state – start to encounter a potential barrier increasing with magnetic field strength (low field seekers), while the other half (high field seekers) encounter a magnetic well. The lowest UCN intensities at  $B = 5$  T are at 57% of the ones at zero magnetic field. That this fraction is considerably larger than one half is because of the improved transmission

of the transported spin state. These UCN have about 300 neV more kinetic energy when passing the AlMg3 window than at B=0.

B(T)	Transmission in 3 s production pulse	Transmission in benchmark pulse
0.0	1.00	1.00
0.5	0.95(3)	0.958(3)
1.0	0.82(2)	0.851(5)
1.5	0.70(1)	0.744(6)
2.0	0.62(1)	0.656(3)
3.0	0.58(1)	0.580(2)
4.0	0.57(1)	0.566(3)
5.0	0.57(1)	0.565(2)

**Table 4.** UCN transmission with respect to magnetic field strength relative to B=0 T, measured with production pulses and benchmark pulses a proton beam current of 2200  $\mu$ A. The larger error in the production pulse measurement reflects the large time jitter of the flapper valve at the time of the measurements. This was largely improved at a later time [24].

#### 4.5.2 UCN rate measurements

Looking into the first 30s of the UCN intensity decrease after production pulses, as shown in Fig. 29, reveals some information about the UCN energy spectrum.

1. The peaks of the count rates, about 1s after the end of the proton pulse, are separated in intensity, as expected, with intensities decreasing with increasing B field. High field seekers and low field seekers with forward momenta high enough to traverse the magnetic field are exiting the beamport.
2. A few seconds after the end of the kick, the UCN rates for  $B = 3, 4$  and 5 T merge. This means, that no high field seekers with forward momenta high enough to traverse  $B = 4$  T magnetic fields are left in the source. A little bit later the same happens for UCNs which cannot traverse  $B = 3$  T. At about 50s after the end of the kick (not shown in Fig. 29), the same happens for UCNs which cannot traverse  $B = 2$  T .

The measurements hence confirms the expected higher loss rates of faster UCN.

A double exponential decay of the form

$$N(t) = ae^{-t/\tau_1} + be^{-t/\tau_2}, \quad (2)$$

where  $N(t)$  is the amount of UCN counted in a given time bin,  $a$  and  $b$  decay amplitudes for the short ( $\tau_1$ ) and long ( $\tau_2$ ) time constants, was fitted to the time spectra. The long time constant is shown in Fig. 30 as a function of

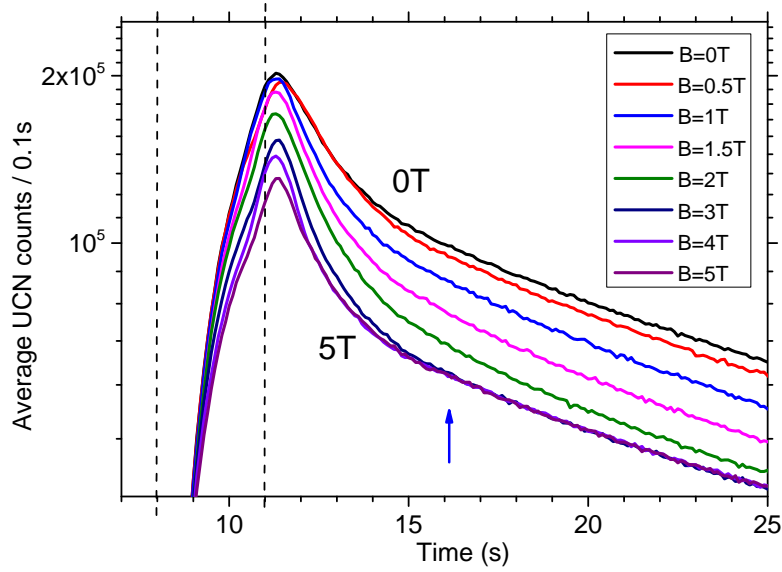


**Figure 29.** Display of UCN rates per 100 ms bins for the first seconds after the proton pulse. The vertical dashed lines indicate start and end times of the 3 s long proton beam kick. The arrow indicates when the rates at  $B = 3, 4$  and  $5$  T merge.

the magnetic field. The fits were done in a time window from 15 s to 300 s, which corresponds to a 285 s long window starting at about 4 s after the end of the proton beam kick.

The long time constant, of the order of 30 s, rises with the magnetic field strength and saturates at 3 T. This is likely because for slower UCN the size of the potential barrier above 3 T does not matter much. In addition the magnetic field reflects low field seekers back into direction to the source. There UCNs can change the spin orientation, e.g. in a wall collision, and then return to the magnet after a diffuse reflection from a wall or from the storage vessel. Like this, some UCN exit the source at later times than in the absence of a magnetic field. This leads to a longer emptying time. A more detailed discussion is given in Sec. 5.4.

## 5 Simulation-based analysis of the measurements

The scope of the present MC analysis is to extract model parameters defined in the established theory of UCN physics in order to characterize the quality of the neutron-optical components, and to identify possible improvements. In all results presented in this paper, the simulated counts represent sampling trajectories and we used free scaling parameters in order to best fit the experimental curves. Computed predictions of the absolute UCN counts at the PSI source will be the subject of a separate forthcoming study.

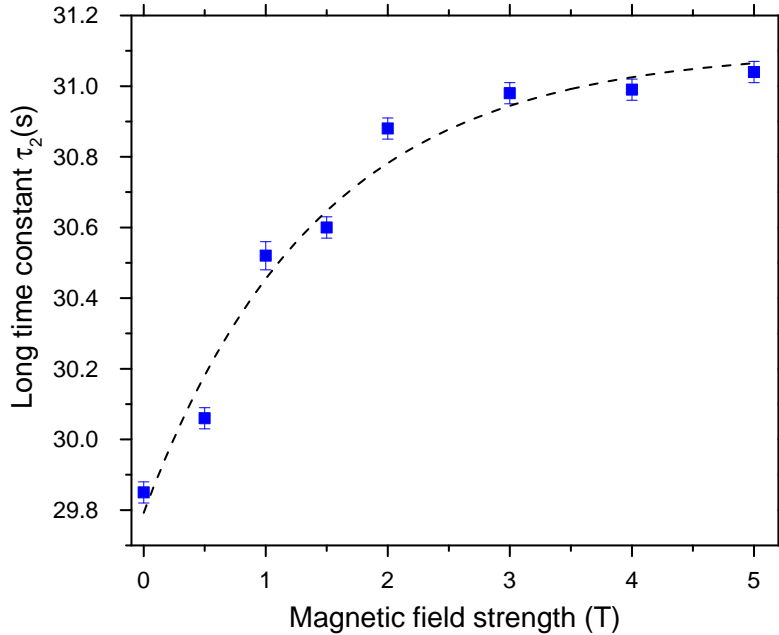


**Figure 30.** Long emptying time constant  $\tau_2$  of the UCN source for different magnetic fields of the polarizing magnet. The values and errors are extracted from fitting double exponential decay curves to the data. The dashed line is to guide the eye.

Our model on diffuse reflections, taking a fraction of reflections as ideally diffuse (Lambertian), is only an approximation. However, for longer time scales which allow for a large number of reflections, storage-effects become important and the concrete mechanism of diffuse reflection will be less relevant. This was demonstrated in several test simulations using alternative diffuse reflection models. Such long time scales are for example our typical emptying and filling times in the experiments comparable to several tens of seconds.

In this sense, in our definition of diffuse reflection properties the diffuse fraction parameter  $p_{\text{diff}}$  is an effective characterization quantity in terms of the Lambert model. We also performed simulations comparing the Lambert and micro-roughness [65] models, e.g. for the case of emptying UCN from a storage chamber into a detector. We obtained almost identical results when setting the Lambert parameter accordingly low (to match micro-roughness) - as a consequence that storage effects were in this case dominant.

Different coating parameters influence with different weights the outcome of measurements or simulations. In some cases it was enough to scan one parameter and compare to the experimental data, the rest of the parameters being irrelevant. For example the calculated storage time constant of the source storage vessel, measured by the counts after UCN traversing the guides and exiting the beamport, is of the order of 100 s, and dominated by the loss parameter. We checked this by performing consistency calculations by varying the diffuse reflection parameters. In order to extract



the UCN guide parameters multidimensional scans were necessary. In each case, single and multi-parameter scans, we also performed several consistency scans by roughly varying parameters which were expected to affect the result less.

### 5.1 Storage vessel parameters

The parameters of the storage vessel of the UCN source were obtained from matching MC results to the storage curves measured via leakage counts (see Sec. 4.1 and Fig. 22). Figure 31 compares MC results with the measurements.

With all shutters closed and setting no gaps in the geometry, the dominating 'loss' channel is represented by the loss parameter within this vessel. In case if possible gaps should be co-represented by this parameter, we call the latter 'effective'. The MC scan gave a fit value for the effective loss parameter of  $(1.5 \pm 0.1) \times 10^{-3}$  for the vessel at room temperature, and  $(1.1 \pm 0.1) \times 10^{-3}$  for the vessel in the cold operating state (around 80 K).

To interpret these large fit values, one must also consider that the effective loss parameter used in the simulation must include all the loss channels possible in the real system. These are (i) nuclear absorption and up-scattering, (ii) losses through gaps along the surface boundaries, and (iii) losses through holes distributed throughout the coated surfaces.

Regarding (i), previous measurements at room temperature [47] yielded an average loss parameter  $\eta$  for DLC on aluminum  $(4 \pm 0.2) \times 10^{-4}$ . At 70 K the measured loss parameter in [47] was  $(1.7 \pm 0.1) \times 10^{-4}$ .

Regard (ii), gaps were found along the borders of individual surfaces (flaps, shutters, wall sections). and measured in the construction phase of the UCN source vessel. About a total of  $25 \text{ cm}^2$  were estimated for the bottom of the vessel, and about the same amount on the side walls. This results in a total gap size of  $50 \text{ cm}^2$  which is a fraction of  $5 \times 10^{-4}$  from all DLC-coated surfaces in the storage vessel. As this was measured at room temperature a large uncertainty might be on this value when comparing to operating conditions.

It was important to check if this gap size is consistent with the measured UCN storage curves. Thus an additional series of simulations was performed. The loss per bounce parameter was set to the measured literature value assuming a very similar surface quality as in [47]. Two gap regions were modeled: (i) an absorbing flat ring on the bottom of the volume around the main flaps, and (ii) an absorbing vertical stripe along one sidewall in the full height of the volume. These two positions represent in the simulation different aspects because of the gradient in UCN density in the storage vessel. In Fig. 32 we plotted density profiles for different times after the pulse start, also indicating the vertical positions of the beamlines. There is also a kinetic energy gradient along the vertical direction due to gravity causing a non-constant bounce-rate and loss probability. The absorbing 'gap' surfaces were set variable. Since the mechanical measurements gave a similar surface of gaps for both the bottom and sidewalls, we kept this ratio during

scanning this simulation parameter. We determined the most probable amount of gaps by minimizing the  $\chi^2$  between the measured and simulated data-points of the storage curve. With this model we also include possible holes in the DLC coating, the aforementioned third loss channel.

The results with the best MC fits were included in Fig. 31. The uncertainty was estimated to 10%. The fitted gap parameter matches very well the gaps determined during the construction i.e. a total of  $50 \pm 5 \text{ cm}^2$  for the warm state. In the cold state of the storage vessel the total gap parameter decreased to  $40 \pm 4 \text{ cm}^2$ , however, remaining compatible with the room-temperature value within the errors. Thermal contraction of aluminum surfaces from 300 K to 100 K would yield only a 1% change, however, depending on the initial size of a gap between the surfaces, this could change by a much larger percentage.

If using a harder UCN energy spectrum than our linear reference spectrum emerging from the UCN converter in the simulations, the fitted loss parameters would shift to slightly lower values. We will study this aspect in the future, after calibrating the initial energy spectrum by a combination of further test measurements and simulations. It is also important to note that a variation of the fraction of diffuse reflections in the storage volume did not make any difference at our level of accuracy.

To conclude, the MC storage curves shown in Fig. 31 well match the ones measured at room temperature and in the cold state (Fig. 26). The simulated storage time constants agree with the measurement within the error bars. Consequently, the linear energy spectrum assumed for UCN exiting from the sD<sub>2</sub> converter was a sufficiently good approximation for this purpose.

## 5.2 UCN guide parameters from emptying time constants

In Figs. 33, 34 and 35 we compare measurement results and MC data. The emptying curve displays the UCN counts decreasing in time after a benchmark pulse or a production pulse. For the case of the South beamline, shown in Fig. 33, the simulation was already validated via parameter scans and fit to the measured slopes. In Fig. 34, the small mismatch in slope between simulation and measurement indicates that the coating parameters obtained for beamline South are not exactly the same as for West-1.

We see a mismatch between MC and measured data at times comparable with the length of the initial proton beam pulse. The agreement is much better at later times when, as discussed above, we expect that the details of the diffuse reflection model is less relevant. During the pulse it is likely that one measures a higher background which is not simulated, mostly from faster (not storable) neutrons which can pass with low probability at small grazing reflection angles along the guides.

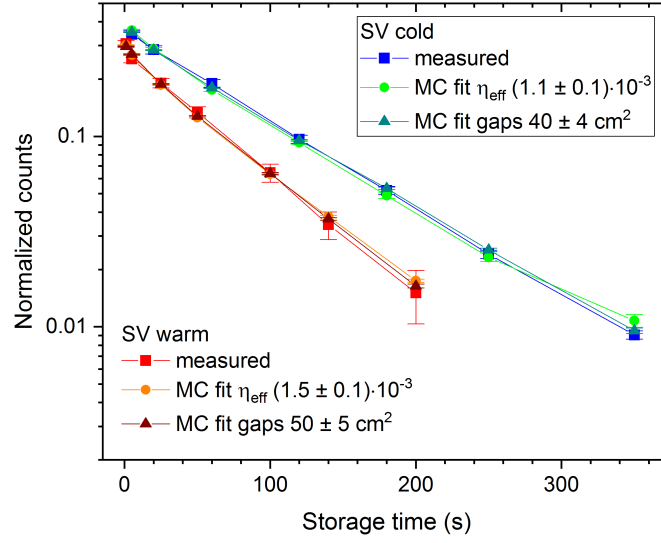


**Figure 31.** Simulation of the storage curve of the UCN source volume for the cold and warm states. First we determined the effective loss parameter  $\eta_{\text{eff}}$  by setting no gaps (orange and green circles, respectively). Then the calculations were redone by setting  $\eta$  to the literature value [47], see text, and scanning the amount of gaps. A total gap of  $50 \text{ cm}^2$  corresponds to a surface fraction of  $5 \times 10^{-4}$ . The filled triangles show the results of simulations with the  $\eta$  from [47] and the best fit gap sizes.

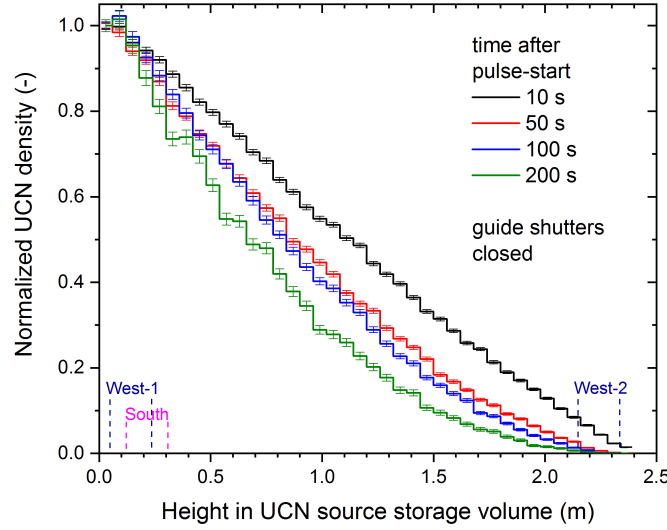


**Figure 32.** Simulated vertical distributions of the UCN density in the UCN source volume ( $h_{\text{max}}=2.4 \text{ m}$ ) for various times after starting the production pulse. The latter in this example lasted 2 s with complete closure of the flapper valve 1 s after the end of the pulse. The density profiles were normalized to the value at the bottom of the vessel. The vertical positions of the three UCN guide exits are indicated. The softening of the UCN spectrum with time is clearly visible. At times close to the measured storage time constant of 90 s in Fig. 31 (see Tab. 3), the half-height density is about one third of the bottom-value.

Another cause of the discrepancy at such short times could be that in reality the low roughness and high roughness surface regions (the latter including cavities at the edges) are unevenly distributed, whereas in the MC model we set uniform surface quality. At short time-scales and, in contrast to what was previously discussed for equilibrium conditions, the implementation of diffuse reflections in the model actually matters. An additional simplification was that the assumed energy spectrum emerging from the UCN converter was linear as obtained from simulations of an

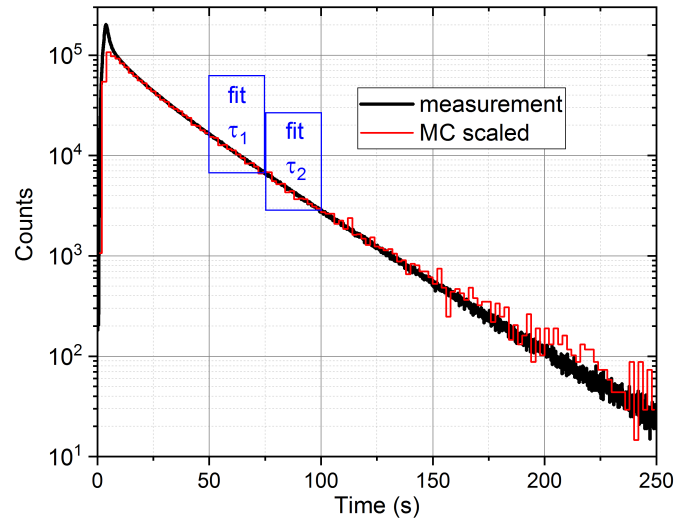


**Figure 33.** Comparison of emptying curves from MC simulations and measured data observed after a 3 s proton beam pulse on UCN guide South. Two time intervals were defined as indicated in the figure and explained in the text. To each interval belongs one time constant,  $\tau_1$  or  $\tau_2$ , from a single-exponential fit. The MC counts were scaled with a free fit parameter to best match the measured counts in the two intervals.

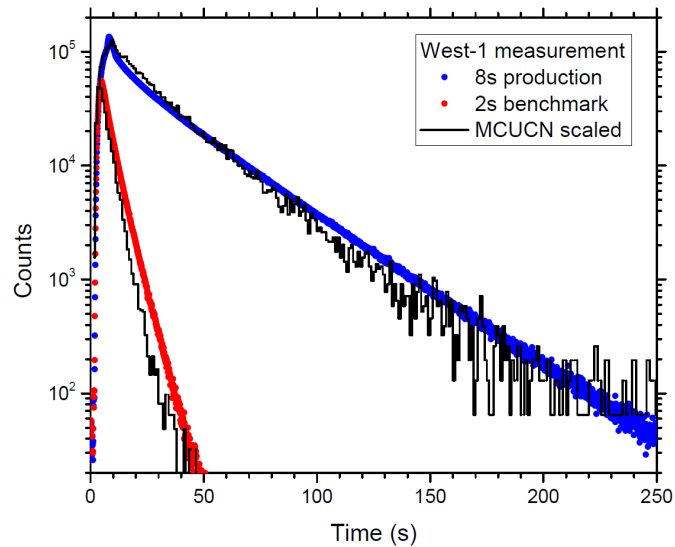


**Figure 34.** Comparison of emptying curve observed on the West-1 beamport in benchmark pulses and production pulses. The MC counts were scaled manually with the same value for both curves to fit the experimental curve of the 8 s pulse in the interval after 50 s similar to the case shown in Figs. 33.

optimal sD<sub>2</sub> structure. If a harder UCN spectrum would be generated, it could enhance the higher energies at early times.

In order to benchmark MC simulations with measurements we compare the emptying time constants which do not depend on the scaling of the UCN counts. We defined two separate time intervals as indicated by the rectangles along the data in Fig. 33, one from 50 s to 75 s, and the next from 75 s to 100 s. Within these short intervals we can safely

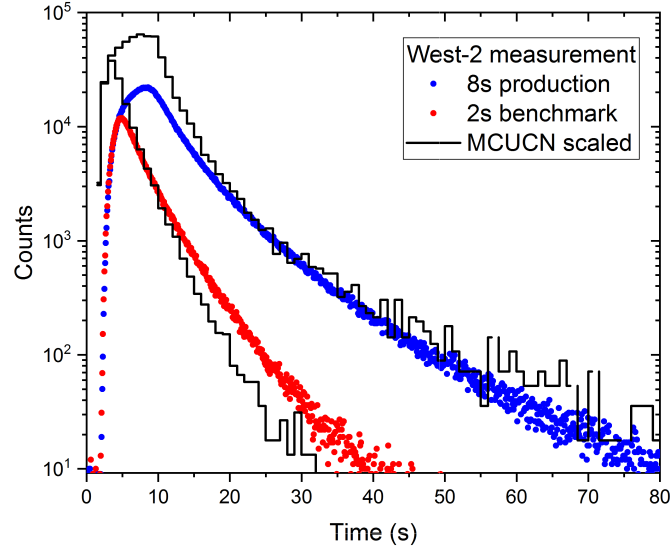


**Figure 35.** Comparison of emptying curves observed on the West-2 beamport in benchmark pulses and production pulses. The MC counts were scaled arbitrarily and independently for the 2 and 8 s pulses in order to compare the slopes visually.

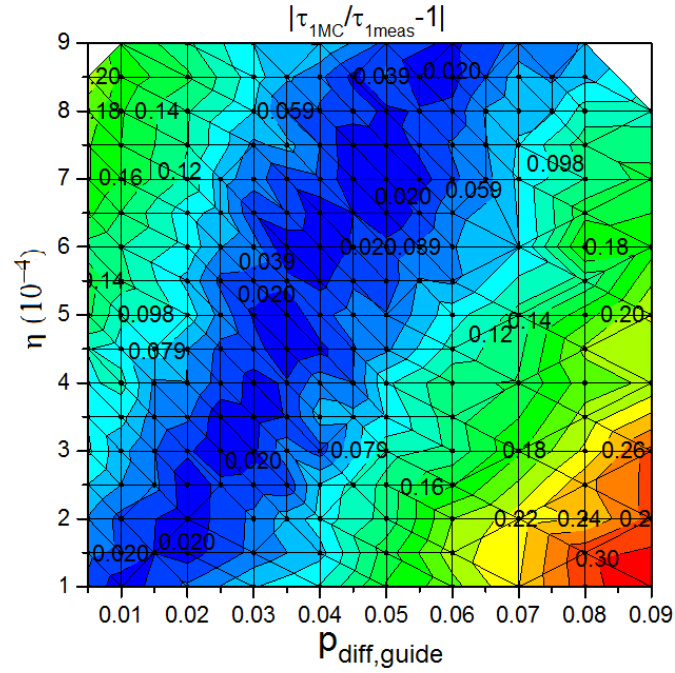


**Figure 36.** Relative deviation plot in the  $\eta - p_{\text{diff,guide}}$  plane between the MC and the experimental emptying time constant  $\tau_1$  (see text). The colors emphasize the contour lines.

assume single-exponential dependence and sufficient statistics for the benchmark. To each interval corresponds one constant,  $\tau_1$  or  $\tau_2$ .

Each of these two time constants were extracted from the measured and the simulated time spectra. We calculated the relative deviation between the MC and the experimental value. The scope is to scan the parameter plane, one axis being the loss parameter  $\eta$  and the other axis the diffuse reflection fraction  $p_{\text{diff,guide}}$ . A single simulation takes ten

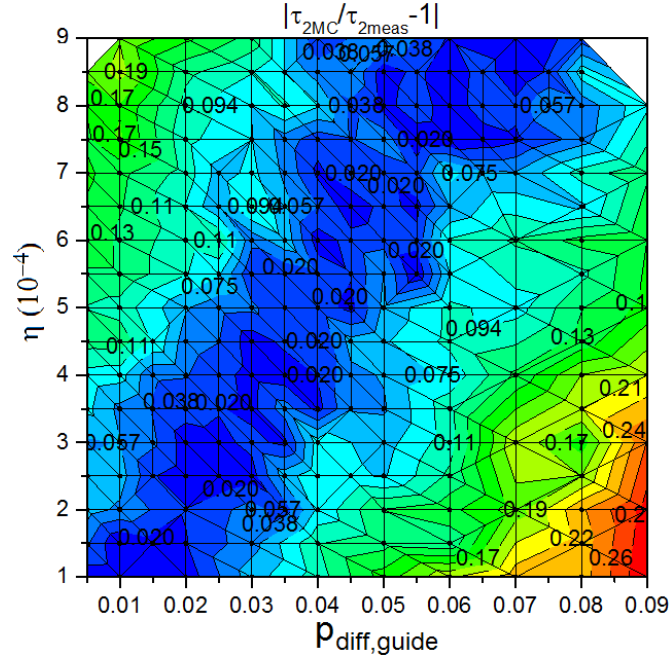


**Figure 37.** Relative deviation plot in the  $\eta - p_{\text{diff,guide}}$  plane between the MC and the experimental emptying time constant  $\tau_2$  (see text). The colors emphasize the contour lines.

minutes in order to produce enough statistics (goal: below 1.5% relative error) for only one parameter configuration. Therefore we scanned along a uniform grid in the parameter space and used triangular interpolation. Thus we obtained a continuous surface of the distribution of the absolute value of the relative deviation on the third axis. Along the third axis we can define contour levels of the deviation.

We interpret the  $1\sigma$  of the measurement and also of the simulation as 68% confidence interval, assuming that the convolution of several uncertainty contributions result in a close-to-normal distribution. Since we have statistical spread on both the measured and the MC values,  $1\sigma$  here is the square root of the sum of squares of each  $1\sigma$  uncertainty.

Figures 36 and 37 show the MC results. These reveal a straight valley with a lowest deviation between MC and measurement reaching down to about 2% with almost connected islands. We take as reference the next level, 4%, which is the first fully connected area. This corresponds to about  $2-3\sigma$  deviation. In the calculations we had a 2% relative statistical spread in the MC counts, and in case of the measurements below 0.4% of the counts.

We observe that the valley of lowest deviation points into a direction in which both parameters grow simultaneously. This is because, in this case, the UCN experience two strongly competing effects: (i) the emptying time-constants are on one hand determined by the speed of emptying, i.e. the transmission quality, but (ii) on the other hand by the loss time constant of the entire storage vessel and neutron guide system. For example, if we increase the loss parameter, the time constant will decrease because we lose UCN much faster. At the same time, if we increase the diffuse parameter we make the emptying slower and thus compensate a faster decay in the time spectrum.

### 5.3 Consistency check by varying the storage volume diffuse fraction

Since the simulations are limited by computation time, we cannot perform very detailed scans by adding those parameters to the parameter space for which we concluded that the dependency of the fit to experiment must be small. However, as a consistency check, we still performed several calculations in which we changed the values of such less relevant parameters.

In Fig. 38 we show a scan to check the variation of the two aforementioned emptying time-constants as a function of the fraction of diffuse reflections at the storage vessel surface. The MC scan was done along a line in the  $\eta - p_{\text{diff,guide}}$  plane across the minimum deviation valley visible in Figs. 36 and 37. Different values for the fraction of diffuse reflections in the storage volume were set. We see a weak dependence of the minimum well on this parameter, however, within the uncertainty of the extracted neutron guide parameters. This confirms the robustness of our results with respect to this parameter.

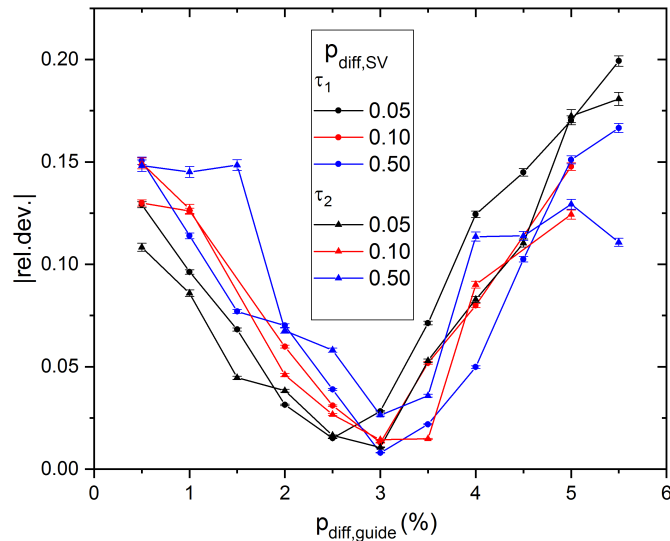


**Figure 38.** Relative deviation of time-constants as a function of the fraction of diffuse reflections in the storage volume,  $p_{\text{diff,SV}}$ . The scan was performed across the  $\eta$  and  $p_{\text{diff,guide}}$  parameter plane of the neutron guides.

### 5.4 UCN intensity variation from the magnetic field of the polarizer

The measurements described in Sec. 4.5 were reproduced satisfactorily by simulations as illustrated in Fig. 28. The low-energy range is not yet well modeled, either because of the not sufficiently well known low-energy spectrum or the not well known transmission of the low-energy UCN. The SC polarizer magnet was simplified to a rectangular

potential profile along the beam axis located at the position of the safety window. Further studies are planned. We also envisage to check how the alternative diffuse reflection models would affect the results.

In Fig. 39 the emptying curves for the case of a 5 T magnetic field are depicted. It can be observed that for time-scales below 50 s the simulation does not reproduce very well the measurement. One cause, which will be checked in further studies, could be that the short time characteristics are determined by the concrete modeling of the diffuse reflections. A Lambert-type modeling turns out to be a too rough approximation for short detection times. It is sufficient only for detection times larger than several tens of seconds as demonstrated in Figs. 33 and 39. The simulations overestimate the time constant for short times as visible in Fig. 40. However, the profile indicating a minimum was qualitatively reproduced. This can be due to the competition of two effects both increasing with the magnetic field: (i) better transmission through the aluminum window allowing for shorter detection times, and (ii) more UCN rejected by the polarizer which depolarize again and have a second chance later to be transmitted, and thus increasing the detection time.

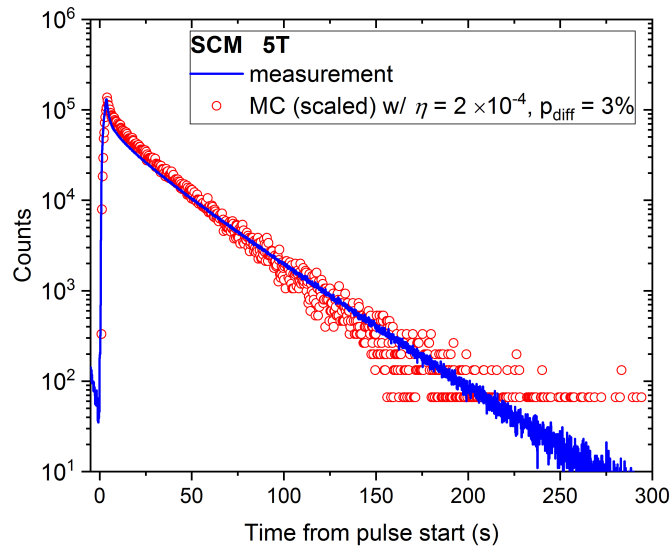


**Figure 39.** Comparison of the measured and simulated emptying curves at 5 T field in the SC magnet.

## 5.5 Simulations of the UCN transmission from the solid deuterium to the beamport

In this section we provide details from simulations describing the dependence of important quantities on time, position, energy, which are not accessible directly from experiments for practical reasons. However, they provide important information on the characteristics of the PSI UCN source and UCN guide system. We obtain information on, for example (i) the time-integrated transmission between the upper surface of the UCN converter and the end of the



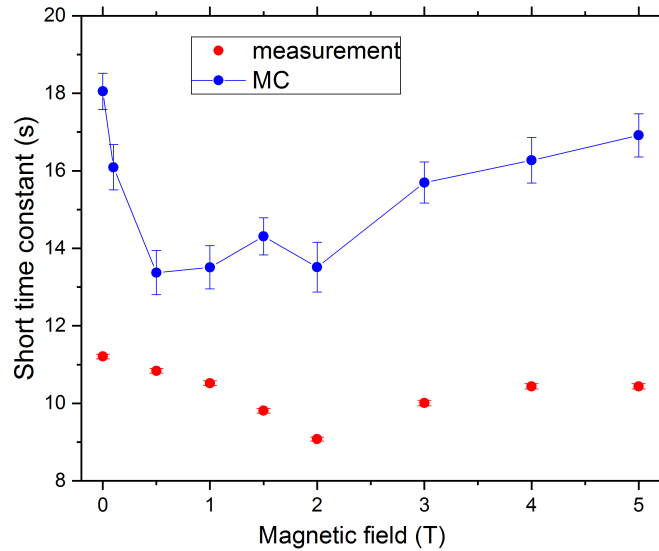


**Figure 40.** MC simulation results and the measured short time constant (Fig. 30) during emptying for a given magnetic field in the SC magnet.

Surface	$V_F$ (neV)	Method	$\eta$ (-)	Method	$p_{\text{diff}}$ (-)	Method	$\Sigma_{\text{atten}}$ $\text{cm}^{-1}\text{m/s}$	Method
Lid sD <sub>2</sub>	54	Al calc.	$1 \times 10^{-4}$	low dep.	0.0	low dep.	49	meas.
Vert. guide	230	NiMo calc.	$5 \times 10^{-4}$	gaps calc.	0.04	low dep.	$\infty$	design
Stor. vessel	230	DLC meas.	$11 \times 10^{-4}$	meas.+MC	0.10	low dep.	$\infty$	design
Guide South	220	NiMo meas.	$3 \times 10^{-4}$	meas. [57] + gaps	0.02	meas.+MC	$\infty$	design
Windows	54	Al calc.	$1 \times 10^{-4}$	low dep.	0.0	low dep.	77	meas.

**Table 5.** Parameters of the coatings used in the simulations: optical potential ( $V_F$ ), loss parameter ( $\eta = W/V_F$ ), fraction of diffuse (Lambert) reflections ( $p_{\text{diff}}$ ), and attenuation constant of the material ( $\Sigma_{\text{atten}}$ ) for 1 m/s. These numbers represent (i) theoretical values [1], (ii) measurements discussed in this paper and in [57], (iii) simulations benchmarked with measurements, (iv) geometrical estimations of gaps, and (v) rough estimations with a low dependency of the outcome.

UCN guides, including the detector window, or (ii) on the energy spectra as a function of time of the detected UCN. Another not accessible observable, the density profile of UCN along the vertical direction in the storage vessel of the UCN source was already plotted in Fig. 32, and helped to estimate the ratio of bounce-rates at different heights.

The parameters for coating quality in the simulation results presented next are summarized in Table 5. We considered the case of direct transmission between the lid above the sD<sub>2</sub> and the detector window, including these two.

In Figs. 41 and 42 the transmission of UCN between the solid deuterium surface and the detector is shown for zero and for 5 T field in the SC polarizer magnet. The transmission was calculated as the ratio of the UCN counts after the detector window, and the number of UCN generated below the lid of the converter vessel, and was separated into bins of the kinetic energy at the level of the beamline axis. The vacuum window of the beamport and that of the detector set the lower energy boundary of the spectrum to the optical potential of aluminum. The different lines indicate successive simulations in which we changed only one parameter at a time (except the random seed). For obvious

reasons the transmission of UCN is strongly energy dependent, thus for a more general purpose, the transmission has to be calculated as a function of energy.

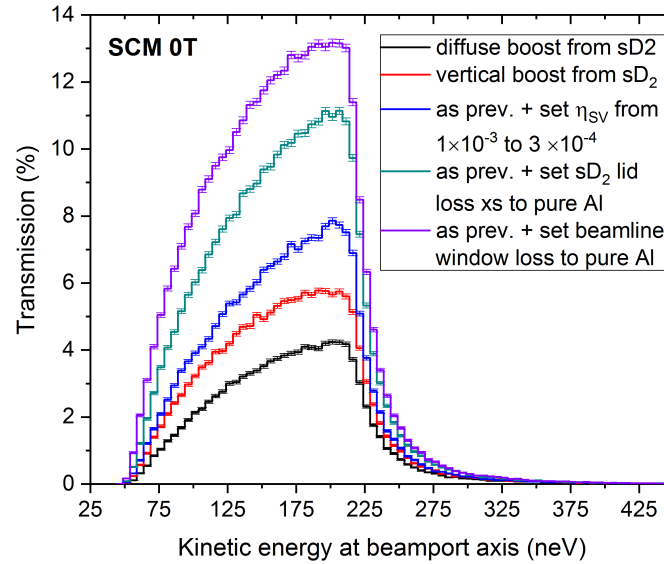


**Figure 41.** Transmission between the UCN converter and detector (including the Al foil of the detector) when the polarizer is switched off. We counted all UCN having the chance to exit the beamport until the next pulse. The kinetic energy is given with respect to the height of the beamport axis.

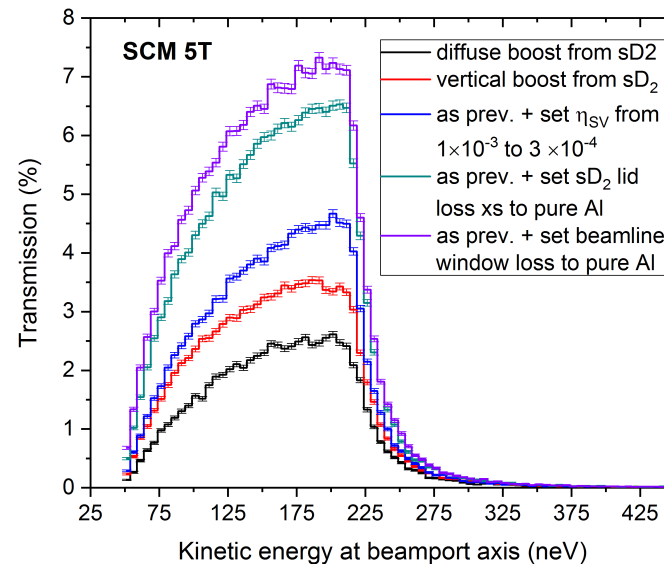


**Figure 42.** Similar as in Fig.41, however, with the SC polarizer at 5 T magnetic field.

In a first step (see the lowest transmission curve in Figs. 41 and 42) the UCN source and guide optics was set as previously benchmarked by matching the test measurements - as described in the above sections - and by setting the energy boost from the solid deuterium diffusely (see Sec. 3.3). This kind of diffuse boost corresponds to the most

probable case when the upper surface of the converter material is very rough, e.g. being composed by poly-crystalline structures, as frost [26].

The next case is the simulation of a vertical boost which would correspond to a perfectly flat surface of the converter material. The gain factor due to this new setting turns out to be about  $1.4 \pm 0.1$ . The latter and next gain factors from these simulations were calculated by averaging in the UCN energy interval 120-230 neV, which is a representative range in which most UCN are transmitted to the beamport (see transmission curves in Fig. 43).

In a second step, we estimate the loss effect due to the gaps in the storage-vessel of the UCN source by changing the effective loss parameter from the one benchmarked above  $1 \times 10^{-3}$  to the pure DLC contribution  $3 \times 10^{-4}$  - as found in measurements [47]. The gain factor obtained in this step is  $1.3 \pm 0.1$ .

The next curves help to localize the loss effects due to the absorption, up-scattering and back-scattering in the vacuum safety windows. It has been shown in [46] and in later comparisons with measurements reported in Section 4.4 and in Ref. [24] that the loss cross-section in the aluminum window is a factor 2.2-2.5 larger than the theoretical value. At first we reduced only the loss cross section in the lid of the converter vessel to the theoretical one. The gain factor due to this new setting is  $1.5 \pm 0.1$ .

The last step was switching the loss parameter in the vacuum safety window to the theoretical one. In this case we see a difference between the two magnetic field settings in the SC polarizer. The gain factor obtained in this step is  $1.3 \pm 0.1$  for field off (un-polarized UCN) and  $1.1 \pm 0.1$  for a 5 T field (polarized UCN). The smaller difference for the case of polarized neutrons was expected because of the energy boost caused by the SC magnet.

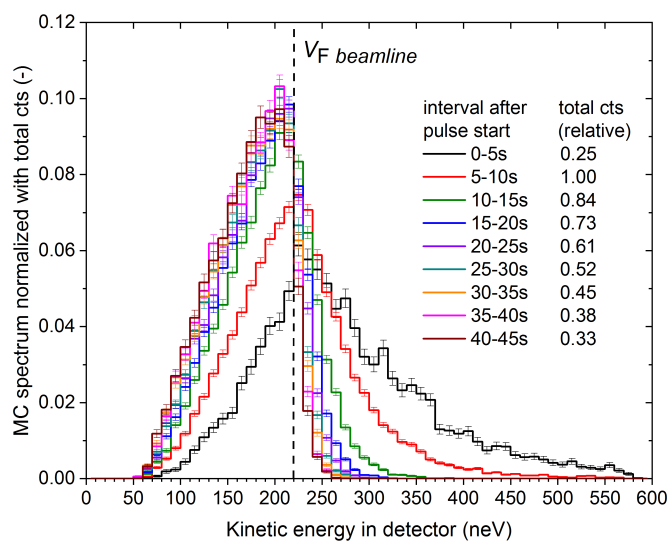


**Figure 43.** UCN counts versus kinetic energy as simulated for a detector at the West-1 beamport. The energy spectra of unpolarized UCN are calculated for different time intervals after the start of the 4 s long proton beam pulse.

The transmission profiles given as a function of UCN energy are valid independently from the initial energy spectrum which was generated at the level of the solid deuterium surface. One can estimate the energy spectra detected at the beamport assuming a linear initial spectrum. The calculations were again considering the case of direct transmission towards the detector. The resulting energy spectra were plotted in Fig. 43 as a function of the time bins after the start of the 4 s proton pulse. The spectra were normalized with their total counts. The change over time in the total counts (relative to the maximum) can be seen in the second column of the figure legend. It can be seen that the spectrum is softening very fast just after the pulse and continues to do so with decreasing rate. The dashed vertical line at 220 neV indicates the optical potential of the UCN guide coating (NiMo) set in the MC simulation. One can clearly see the decrease in the spectra above this energy limit. At short times a large fraction of very-cold neutrons (in our case with energies higher than 220 neV) are still present. Even after 30 s the fraction of these faster neutrons is not negligible compared to the area of the same curve below the 220 neV threshold.

We can conclude that MC simulations help us to quantify several effects causing UCN losses in the PSI UCN source and guide system. Just after the proton pulse there is a considerable amount of neutrons faster than UCN, which could be important for specific applications.

## 6 Summary

This paper presents all components which define the ultracold neutron optics of the PSI UCN source. UCN intensities and their increase in subsequent years are given. Measurements of storage time constants, of UCN intensities and their time dependence, and of UCN transmissions are shown as relevant characterization measurements. Together with measurements characterizing the UCN surfaces they define the neutron optics parameters of the source.

The MCUCN simulation model together with dedicated experiments allowed for constraining overall quality parameters characterizing the optical components above the main shutter of the UCN source vessel. A specific characterization of the vertical guide part of the source will be the subject of a forthcoming study. The resulting cross-checked simulation allowed the calculation of relevant parameters of the UCN source which are not accessible to experiments, like the UCN density distribution in the storage vessel. The presented results demonstrate the excellent performance of the PSI UCN source and will help us to better understand and further optimize its performance.

## Acknowledgments

All people who have been contributing to design and construction of the PSI UCN source are gratefully acknowledged. The outstanding continuous technical support of M. Meier and F. Burri is acknowledged. We are grateful to the BSQ group operating the UCN source, namely P. Erisman, R. Erne, K. Geissmann, A. Kalt, T. Hofmann, J. Welte and D. Viol. Operations support by A. Anghel is appreciated. We acknowledge the excellent support by the PSI proton accelerator operations section, especially A. Mezger and D. Reggiani, and the target group of M. Wohlmuther and V. Talanov, and the excellent support by many other PSI support groups. Personal efforts and support of P. Bucher, U. Bugmann, M. Dänzer, J. Ehrat, A. Fuchs, A. Gnädinger, A. Hirt, M. Horisberger, B. Jehle, R. Käch, R. Knecht, M. Koller, M. Mähr, O. Morath, M. Müller, W. Pfister, P. Rüttimann, R. Schelldorfer, T. Stapf and C. Stettler are acknowledged. This work was supported by the Swiss National Science Foundation Projects 200020\_137664 and 200020\_149813, 200020\_163413. Special thanks for granting access to the PL-Grid [66].

## References

1. R. Golub, D.J. Richardson, and S.K. Lamoreaux. *Ultra-Cold Neutrons*. Adam Hilger, Bristol, Philadelphia, and New York, 1991.
2. V.K. Ignatovich. *The Physics of Ultracold Neutrons*. Oxford Science Publishing, Clarendon, Oxford, 1990.
3. M. Utsuro and V.K. Ignatovich. *Handbook of neutron optics*. Wiley-VCH Verlag GmbH & Co, 2010.
4. C. A. Baker, D. D. Doyle, P. Geltenbort, K. Green, M. G. D. van der Grinten, P. G. Harris, P. Iaydjiev, S. N. Ivanov, D. J. R. May, J. M. Pendlebury, J. D. Richardson, D. Shiers, and K. F. Smith. Improved experimental limit on the electric dipole moment of the neutron. *Phys. Rev. Lett.*, 97(13):131801, September 2006.
5. C.A. Baker, G. Ban, K. Bodek, M. Burghoff, Z. Chowdhuri, M. Daum, M. Fertl, B. Franke, P. Geltenbort, K. Green, M.G.D. van der Grinten, E. Gutmiedl, P.G. Harris, R. Henneck, P. Iaydjiev, S.N. Ivanov, N. Khomutov, M. Kasprzak, K. Kirch, S. Kistryn, S. Knappe-Gruneberg, A. Knecht, P. Knowles, A. Kozela, B. Lauss, T. Lefort, Y. Lemièrre, O. Naviliat-Cuncic, J.M. Pendlebury, E. Pierre, F.M. Piegsa, G. Pignol, G. Quemener, S. Rocchia, P. Schmidt-Wellenburg, D. Shiers, K.F. Smith, A. Schnabel, L. Trahms, A. Weis, J. Zejma, J. Zenner, and G. Zsigmond. The search for the neutron electric dipole moment at the Paul Scherrer Institute. *Physics Proc.*, 17(0):159 – 167, 2011. 2nd International Workshop on the Physics of fundamental Symmetries and Interactions - PSI2010.
6. A. P. Serebrov, E. A. Kolomenskiy, A. N. Pirozhkov, I. A. Krasnoschekova, A. V. Vassiljev, A. O. Polyushkin, M. S. Lasakov, A. N. Murashkin, V. A. Solovey, A. K. Fomin, I. V. Shoka, O. M. Zhrebtsov, P. Geltenbort, S. N. Ivanov, O. Zimmer,

- E. B. Alexandrov, S. P. Dmitriev, and N. A. Dovator. New search for the neutron electric dipole moment with ultracold neutrons at ILL. *Phys. Rev. C*, 92:055501, Nov 2015.
7. J. M. Pendlebury, S. Afach, N. J. Ayres, C. A. Baker, G. Ban, G. Bison, K. Bodek, M. Burghoff, P. Geltenbort, K. Green, W. C. Griffith, M. van der Grinten, Z. D. Grujić, P. G. Harris, V. H elaine, P. Iaydjiev, S. N. Ivanov, M. Kasprzak, Y. Kermaidic, K. Kirch, H.-C. Koch, S. Komposch, A. Kozela, J. Krempel, B. Lauss, T. Lefort, Y. Lemi ere, D. J. R. May, M. Musgrave, O. Naviliat-Cuncic, F. M. Piegsa, G. Pignol, P. N. Prashanth, G. Qu em ener, M. Rawlik, D. Rebreyend, J. D. Richardson, D. Ries, S. Roccia, D. Rozpedzik, A. Schnabel, P. Schmidt-Wellenburg, N. Severijns, D. Shiers, J. A. Thorne, A. Weis, O. J. Winston, E. Wursten, J. Zejma, and G. Zsigmond. Revised experimental upper limit on the electric dipole moment of the neutron. *Phys. Rev. D*, 92:092003, Nov 2015.
  8. C. Abel, N. J. Ayres, G. Ban, G. Bison, K. Bodek, V. Bondar, M. Daum, M. Fairbairn, V. V. Flambaum, P. Geltenbort, K. Green, W. C. Griffith, M. van der Grinten, Grujic Z. D., P. G. Harris, N. Hild, P. Iaydjiev, S. N. Ivanov, M. Kasprzak, Y. Kermaidic, K. Kirch, H.-C. Koch, S. Komposch, P. A. Koss, A. Kozela, J. Krempel, B. Lauss, T. Lefort, Y. Lemiere, D. J. E. Marsh, P. Mohanmurthy, A. Mtchedlishvili, M. Musgrave, F. M. Piegsa, G. Pignol, M. Rawlik, D. Rebreyend, D. Ries, S. Roccia, D. Rozpedzik, P. Schmidt-Wellenburg, N. Severijns, D. Shiers, Y. V. Stadnik, A. Weis, E. Wursten, J. Zejma, and G. Zsigmond. Search for axionlike dark matter through nuclear spin precession in electric and magnetic fields. *Phys. Rev. X*, 7(4):041034–, 2017.
  9. Ameya Kolarkar. Search for the Neutron Electric Dipole Moment at the SNS at Oak Ridge. *AIP Conf. Proc.*, 1200:861–864, 2010.
  10. J. W. Martin and Japan-Canada nEDM Collaboration. TRIUMF facility for a neutron electric dipole moment experiment. *AIP Conference Proceedings*, 1560(1):134–136, October 2013.
  11. F.E. Wietfeldt and G.L. Greene. The neutron lifetime. *Rev. Mod. Phys.*, 83:1173–1192, 2011.
  12. A. T. Yue, M. S. Dewey, D. M. Gilliam, G. L. Greene, A. B. Laptev, J. S. Nico, W. M. Snow, and F. E. Wietfeldt. Improved determination of the neutron lifetime. *Phys. Rev. Lett.*, 111(22):222501–, November 2013.
  13. A. P. Serebrov, E. A. Kolomensky, A. K. Fomin, I. A. Krasnoshchekova, A. V. Vassiljev, D. M. Prudnikov, I. V. Shoka, A. V. Chechkin, M. E. Chaikovskiy, V. E. Varlamov, S. N. Ivanov, A. N. Pirozhkov, P. Geltenbort, O. Zimmer, T. Jenke, M. Van der Grinten, and M. Tucker. Neutron lifetime measurements with a large gravitational trap for ultracold neutrons. *Phys. Rev. C*, 97(5):055503–, May 2018.
  14. R. W. Pattie, N. B. Callahan, C. Cude-Woods, E. R. Adamek, L. J. Broussard, S. M. Clayton, S. A. Currie, E. B. Dees, X. Ding, E. M. Engel, D. E. Fellers, W. Fox, P. Geltenbort, K. P. Hickerson, M. A. Hoffbauer, A. T. Holley, A. Komives, C.-Y. Liu, S. W. T. MacDonald, M. Makela, C. L. Morris, J. D. Ortiz, J. Ramsey, D. J. Salvat, A. Saunders, S. J. Seestrom, E. I. Sharapov, S. K. Sjue, Z. Tang, J. Vanderwerp, B. Vogelaar, P. L. Walstrom, Z. Wang, W. Wei, H. L. Weaver, J. W.

- Wexler, T. L. Womack, A. R. Young, and B. A. Zeck. Measurement of the neutron lifetime using a magneto-gravitational trap and in situ detection. *Science*, 6389:627–632, May 2018.
15. K. Kirch, B. Lauss, P. Schmidt-Wellenburg, and G. Zsigmond. Ultracold neutrons - physics and production. *Nucl. Phys. News*, 20:17–23, 2010.
  16. G. Bison, M. Daum, K. Kirch, B. Lauss, D. Ries, P. Schmidt-Wellenburg, G. Zsigmond, T. Brenner, P. Geltenbort, T. Jenke, O. Zimmer, M. Beck, W. Heil, J. Kahlenberg, J. Karch, K. Ross, K. Eberhardt, C. Geppert, S. Karpuk, T. Reich, C. Siemenssen, Y. Sobolev, and N. Trautmann. Comparison of ultracold neutron sources for fundamental physics measurements. *Phys. Rev. C*, 95(4):045503, 2017.
  17. A. Anghel, F. Atchison, B. Blau, B. van den Brandt, M. Daum, R. Doelling, M. Dubs, P.-A. Duperrex, A. Fuchs, D. George, L. Göttl, P. Hautle, G. Heidenreich, F. Heinrich, R. Henneck, S. Heule, Th. Hofmann, St. Joray, M. Kasprzak, K. Kirch, A. Knecht, J.A. Konter, T. Korhonen, M. Kuzniak, B. Lauss, A. Mezger, A. Mtchedlishvili, G. Petzoldt, A. Pichlmaier, D. Reggiani, R. Reiser, U. Rohrer, M. Seidel, H. Spitzer, K. Thomsen, W. Wagner, M. Wohlmuther, G. Zsigmond, J. Zuellig, K. Bodek, S. Kistryn, J. Zejma, P. Geltenbort, C. Plonka, and S. Grigoriev. The PSI ultra-cold neutron source. *Nucl. Instrum. Methods A*, 611:272–275, 2009.
  18. B. Lauss. A new facility for fundamental particle physics: The high-intensity ultracold neutron source at the Paul Scherrer Institute. *AIP Conf. Proc.*, 1441(1):576–578, 2012.
  19. B. Lauss. Startup of the high-intensity ultracold neutron source at the Paul Scherrer Institute. *Hyperf. Int.*, 211:21–25, 2012.
  20. B. Lauss. Ultracold Neutron Production at the Second Spallation Target of the Paul Scherrer Institute. *Phys. Proc.*, 51:98, 2014.
  21. H. Becker, G. Bison, B. Blau, Z. Chowdhuri, J. Eikenberg, M. Fertl, K. Kirch, B. Lauss, G. Perret, D. Reggiani, D. Ries, P. Schmidt-Wellenburg, V. Talanov, M. Wohlmuther, and G. Zsigmond. Neutron production and thermal moderation at the PSI UCN source. *Nucl. Instrum. Methods A*, 777(0):20–27, 2015.
  22. B. Blau, M. Daum, M. Fertl, P. Geltenbort, L. Goeltl, R. Henneck, K. Kirch, A. Knecht, B. Lauss, P. Schmidt-Wellenburg, and G. Zsigmond. A prestorage method to measure neutron transmission of ultracold neutron guides. *Nucl. Instrum. Methods A*, 807:30 – 40, 2016.
  23. L. Göttl. *Characterization of the PSI ultra-cold neutron source*. PhD thesis, ETH Zürich, No.20350, 2012.
  24. D. Ries. *Characterisation and Optimisation of the Source for Ultracold Neutrons at the Paul Scherrer Institute*. PhD thesis, ETH Zürich, No.23671, 2016.
  25. G. Zsigmond. The MCUCN simulation code for ultracold neutron physics. *Nucl. Instrum. Methods A*, 881:16–26, 2018.
  26. A. Anghel, T. L. Bailey, G. Bison, B. Blau, L. J. Broussard, S. M. Clayton, C. Cude-Woods, M. Daum, A. Hawari, N. Hild, P. Huffman, T. M. Ito, K. Kirch, E. Korobkina, B. Lauss, K. Leung, E. M. Lutz, M. Makela, G. Medlin, C. L. Morris, R. W.

- Pattie, D. Ries, A. Saunders, P. Schmidt-Wellenburg, V. Talanov, A. R. Young, B. Wehring, C. White, M. Wohlmuther, and G. Zsigmond. Solid deuterium surface degradation at ultracold neutron sources. *The European Physical Journal A*, 54(9):148–, 2018.
27. A. Anghel, B. Blau, Daum M., Kirch K., and Grigoriev S. Cryogenic system of the Swiss ultra-cold neutron source. In *Proc. of the 10th IIR International Conference Cryogenics, 04/21-04/25, 2008, Prague, Czech Republic*, 2008.
28. K. van der Meer, M.B. Goldberg, E.H. Lehmann, H. A. Abderrahim, D. Bar, D. Berkovits, M. Daum, S. Dekelver, Y. Foucher, J. Gerber, F. Van Gestel, W. Hajdas, H.-P. Linder, E. Malambu, I. Mardor, J. Oeyen, D. Saphier, A. Shor, M. Willekens, and Y. Yariv. Spallation yields of neutrons produced in thick lead/bismuth targets by protons at incident energies of 420 and 590 MeV. *Nuclear Instrum. Methods B*, 217(2):202–220, 2004.
29. M. Wohlmuther and G. Heidenreich. The spallation target of the ultra-cold neutron source UCN at PSI. *Nucl. Instrum. Methods A*, 564:51, 2006.
30. D. Anicic, M. Daum, G. Dzieglewski, D. George, M. Horvat, G. Janser, F. Jenni, I. Jirousek, K. Kirch, T. Korhonen, R. Kuenzi, A.C. Mezger, U. Rohrer, and L. Tanner. A fast kicker magnet for the PSI 600MeV proton beam to the PSI ultra-cold neutron source. *Nucl. Instrum. Method. A*, 541(3):598–609, 2005.
31. F. Atchison, P. Baumann, T. Brys, M. Daum, A. Egorov, P. Fierlinger, P. Fuchs, R. Henneck, St. Joray, R. Keil, K. Kirch, R. Krutova, G. Kuehne, V.T. Lebedev, H. Obermeier, D.N. Orlova, Ch. Perret, A. Pichlmaier, Ph. Richard, A. Serebrov, and S. Thies. On the use of lead/tin alloys as target material for the production of spallation neutrons. *Nucl. Instrum. Methods A*, 539(3):646–653, 2005.
32. R. Golub and J.M. Pendlebury. The interaction of Ultra-Cold Neutrons (UCN) with liquid helium and a superthermal UCN source. *Phys. Lett. A*, 62(5):337–339, 1977.
33. A. P. Serebrov, V. A. Mityukhlyaev, A. A. Zakharov, A.G. Kharitonov, V.V. Nesvizhesvsky, M.S. Lasakov, R.R. Tal'daev, A.V. Aldushchenkov, A.V. Varlamov, V.E. and Vasil'ev, G. Greene, and T. Bowles. Experimental study of a solid-deuterium source of ultracold neutrons. *JETP Lett.*, 62:785, 1995.
34. A. P. Serebrov, V. A. Mityukhlyaev, A. A. Zakharov, T. Bowles, G. Greene, and J. Sromicki. Solid deuterium source of ultracold neutrons based on a pulsed spallation source. *JETP Lett.*, 66:802–808, 1997.
35. A. Serebrov, V. Mityukhlyaev, A. Zakharov, A. Kharitonov, V. Shustov, V. Kuz'minov, M. Lasakov, R. Tal'daev, A. Aldushchenkov, V. Varlamov, A. Vasil'ev, M. Sazhin, G. Greene, T. Bowles, R. Hill, S. Seestrom, and P. Geltenbort. Studies of a solid-deuterium source for ultra-cold neutrons. *Nucl. Instrum. Methods A*, 440(3):658–665, 2000.
36. A.P. Serebrov, E. A. Kolomenski, M. S. Lasakov, V. A. Mityukhlyaev, A. N. Pirozhkov, I. A. Potapov, E. Varlamov, A. V. Vasliev, Young A. R., and A. Zakharov. Experimental studies of very cold neutrons passing through solid deuterium. *JETP Lett.*, 74:302, 2001.



37. C. L. Morris, J. M. Anaya, T. J. Bowles, B. W. Filippone, P. Geltenbort, R. E. Hill, M. Hino, S. Hoedl, G. E. Hogan, T. M. Ito, T. Kawai, K. Kirch, S. K. Lamoreaux, C.-Y. Liu, M. Makela, L. J. Marek, J. W. Martin, R. N. Mortensen, A. Pichlmaier, A. Saunders, S. J. Seestrom, D. Smith, W. Teasdale, B. Tipton, M. Utsuro, A. R. Young, and J. Yuan. Measurements of ultracold-neutron lifetimes in solid deuterium. *Phys. Rev. Lett.*, 89(27):272501, 2002.
38. A. Saunders, J.M. Anaya, T.J. Bowles, B.W. Filippone, P. Geltenbort, R.E. Hill, M. Hino, S. Hoedl, G.E. Hogan, T.M. Ito, K.W. Jones, T. Kawai, K. Kirch, S.K. Lamoreaux, C.-Y. Liu, M. Makela, L.J. Marek, J.W. Martin, C.L. Morris, R.N. Mortensen, A. Pichlmaier, S.J. Seestrom, A. Serebrov, D. Smith, W. Teasdale, B. Tipton, R.B. Vogelaar, A.R. Young, and J. Yuan. Demonstration of a solid deuterium source of ultra-cold neutrons. *Phys. Lett. B*, 593(1-4):55-60, July 2004.
39. K. Bodek, B. van den Brandt, T. Brys, M. Daum, P. Fierlinger, P. Geltenbort, M. Giersch, P. Hautle, R. Henneck, M. Kasprzak, K. Kirch, J.A. Konter, G. Kuehne, M. Kuzniak, K. Mishima, A. Pichlmaier, D. Raetz, A. Serebrov, and J. Zmeskal. An apparatus for the investigation of solid D2 with respect to ultra-cold neutron sources. *Nucl. Instrum. Methods A*, 533:491-504, 2004.
40. F. Atchison, B. van den Brandt, T. Brys, M. Daum, P. Fierlinger, P. Hautle, R. Henneck, S. Heule, M. Kasprzak, K. Kirch, J. A. Konter, A. Michels, A. Pichlmaier, M. Wohlmuther, A. Wokaun, K. Bodek, U. Szerer, P. Geltenbort, J. Zmeskal, and Y. Pokotilovskiy. Production of ultracold neutrons from a cold neutron beam on a  $^2\text{H}_2$  target. *Phys. Rev. C*, 71(5):054601, May 2005.
41. F. Atchison, B. van den Brandt, T. Brys, M. Daum, P. Fierlinger, P. Hautle, R. Henneck, S. Heule, M. Kasprzak, K. Kirch, J. A. Konter, A. Michels, A. Pichlmaier, M. Wohlmuther, A. Wokaun, K. Bodek, U. Szerer, P. Geltenbort, J. Zmeskal, and Y. Pokotilovskiy. Measured total cross sections of slow neutrons scattered by gaseous and liquid  $^2\text{H}_2$ . *Phys. Rev. Lett.*, 94:212502, 2005.
42. F. Atchison, B. Blau, B. van den Brandt, T. Brys, M. Daum, P. Fierlinger, P. Hautle, R. Henneck, S. Heule, M. Kasprzak, K. Kirch, J. Kohlbrecher, G. Kuehen, J. A. Konter, A. Pichlmaier, A. Wokaun, K. Bodek, P. Geltenbort, and J. Zmeskal. Measured total cross sections of slow neutrons scattered by solid deuterium and implications for ultracold neutron sources. *Phys. Rev. Lett.*, 95:182502, 2005.
43. F. Atchison, B. Blau, K. Bodek, B. van den Brandt, T. Brys, M. Daum, P. Fierlinger, A. Frei, P. Geltenbort, P. Hautle, R. Henneck, S. Heule, A. Holley, M. Kasprzak, K. Kirch, A. Knecht, J. A. Konter, M. Kuzniak, C.-Y. Liu, C. L. Morris, A. Pichlmaier, C. Plonka, Y. Pokotilovski, A. Saunders, Y. Shin, D. Tortorella, M. Wohlmuther, A. R. Young, J. Zejma, and G. Zsigmond. Cold neutron energy dependent production of ultracold neutrons in solid deuterium. *Phys. Rev. Lett.*, 99(26):262502, 2007.
44. F. Atchison, B. Blau, K. Bodek, B. van den Brandt, T. Brys, M. Daum, P. Fierlinger, A. Frei, P. Geltenbort, P. Hautle, R. Henneck, S. Heule, A. Holley, M. Kasprzak, K. Kirch, A. Knecht, J.A. Konter, M. Kuzniak, C.-Y. Liu, C.L. Morris,

- A. Pichlmaier, C. Plonka, Y. Pokotilovski, A. Saunders, Y. Shin, D. Tortorella, M. Wohlmuther, A.R. Young, J. Zejma, and G. Zsigmond. Production of ultracold neutrons from cryogenic  $2\text{H}_2$ ,  $\text{O}_2$ , and  $\text{C}_2\text{H}_4$  converters. *Eur.Phys.Lett*, 95:1, 2011.
45. I. Altarev, F. Atchison, M. Daum, A. Frei, E. Gutmiedl, G. Hampel, F. J. Hartmann, W. Heil, A. Knecht, J. V. Kratz, T. Lauer, M. Meier, S. Paul, Y. Sobolev, and N. Wiehl. Direct experimental verification of neutron acceleration by the material optical potential of solid  $^2\text{H}_2$ . *Phys. Rev. Lett.*, 100(1):014801–, 2008.
46. F. Atchison, Blau B., A. Bollhalder, M. Daum, P. Fierlinger, P. Geltenbort, and G. Hampel. Transmission of very slow neutrons through material foils and its influence on the design of ultracold neutron sources. *Nucl. Instrum. Methods A*, A 608:144–151, 2009.
47. F. Atchison, T. Brys, M. Daum, P. Fierlinger, P. Geltenbort, R. Henneck, S. Heule, M. Kasprzak, K. Kirch, A. Pichlmaier, C. Plonka, U. Straumann, and C. Wermelinger. First storage of ultracold neutrons using foils coated with diamond-like carbon. *Phys. Lett. B*, 625:19–25, 2005.
48. F. Atchison, B. Blau, M. Daum, P. Fierlinger, A. Foelske, P. Geltenbort, M. Gupta, R. Henneck, S. Heule, M. Kasprzak, M. Kuzniak, K. Kirch, M. Meier, A. Pichlmaier, C. Plonka, R. Reiser, B. Theiler, O. Zimmer, and G. Zsigmond. Diamond-like carbon can replace beryllium in physics with ultracold neutrons. *Phys. Lett. B*, 642:24–27, 2006.
49. F. Atchison, B. Blau, M. Daum, P. Fierlinger, P. Geltenbort, R. Henneck, S. Heule, M. Kasprzak, K. Kirch, K. Kohlik, M. Kuzniak, M. Meier, C.-F. Meyer, A. Pichlmaier, C. Plonka, P. Schmidt-Wellenburg, B. Schultrich, Th. Stucky, V. Weihnacht, and O. Zimmer. Storage of ultracold neutrons in a volume coated with diamondlike carbon. *Phys. Rev. C*, 74:055501, 2006.
50. F. Atchison, T. Brys, M. Daum, P. Fierlinger, P. Geltenbort, R. Henneck, S. Heule, M. Kasprzak, K. Kirch, A. Pichlmaier, C. Plonka, U. Straumann, C. Wermelinger, and G. Zsigmond. Loss and spinflip probabilities for ultracold neutrons interacting with diamondlike carbon and beryllium surfaces. *Phys. Rev. C*, 76(4):044001, 2007.
51. F. Atchison, T. Brys, M. Daum, P. Fierlinger, A. Foelske, M. Gupta, R. Henneck, S. Heule, M. Kasprzak, K. Kirch, R. KÄütz, M. Kuzniak, T. Lippert, C.-F. Meyer, F. Nolting, A. Pichlmaier, D. Schneider, B. Schultrich, P. Siemroth, and U. Straumann. Structural characterization of diamond-like carbon films for ultracold neutron applications. *Diamond and Related Materials*, 16:334–341, 2007.
52. F. Atchison, A. Bergmaier, M. Daum, M. Doebeli, G. Dollinger, P. Fierlinger, A. Foelske, R. Henneck, S. Heule, M. Kasprzak, K. Kirch, A. Knecht, M. Kuzniak, A. Pichlmaier, R. Schelldorfer, and G. Zsigmond. Surface characterization of diamond-like carbon for ultracold neutron storage. *Nucl. Instrum. Methods A*, 587(1):82–88, 2008.
53. K. Bodek, M. Daum, R. Henneck, S. Heule, M. Kasprzak, K. Kirch, A. Knecht, M. Kuźniak, B. Lauss, M. Meier, G. Petzoldt, M. Schneider, and G. Zsigmond. Storage of ultracold neutrons in high resistivity, non-magnetic materials with high Fermi potential. *Nucl. Instrum. Methods A*, 597:222–226, 2008.

54. F. Atchison, M. Daum, R. Henneck, S. Heule, M. Horisberger, M. Kasprzak, K. Kirch, A. Knecht, M. Kuzniak, B. Lauss, A. Mtchedlishvili, M. Meier, G. Petzoldt, C. Plonka-Spehr, R. Schelldorfer, U. Straumann, and G. Zsigmond. Diffuse reflection of ultracold neutrons from low-roughness surfaces. *The European Physical Journal A*, 44(1):23–29, 2010.
55. J. Bertsch, L. Göttl, K. Kirch, B. Lauss, and R. Zubler. Neutron radiation hardness of vacuum compatible two-component adhesives. *Nucl. Instrum. Methods A*, 602(2):552–556, 2009.
56. L. Göttl, Z. Chowdhuri, M. Fertl, F. Gray, R. Henneck, K. Kirch, B. Lauss, T. Lefort, A. Mtchedlishvili, P. Schmidt-Wellenburg, and G. Zsigmond. An endoscopic detector for ultracold neutrons. *Eur. Phys. J. A*, 49(9), 2013.
57. V. Bondar, S. Chesnevskaia, M. Daum, B. Franke, P. Geltenbort, L. Goeltl, E. Gutmiedl, J. Karch, M. Kasprzak, G. Kessler, K. Kirch, H.-C. Koch, A. Kraft, T. Lauer, B. Lauss, E. Pierre, G. Pignol, D. Reggiani, P. Schmidt-Wellenburg, Yu. Sobolev, T. Zechlau, and G. Zsigmond. Losses and depolarization of ultracold neutrons on neutron guide and storage materials. *Phys. Rev. C*, 96(3):035205–, 2017.
58. I. Altarev, M. Daum, A. Frei, E. Gutmiedl, G. Hampel, F. J. Hartmann, W. Heil, A. Knecht, J. V. Kratz, T. Lauer, M. Meier, S. Paul, U. Schmidt, Y. Sobolev, N. Wiehl, and G. Zsigmond. Neutron velocity distribution from a superthermal solid 2H<sub>2</sub> ultracold neutron source. *Eur. Phys. J. A*, 37(1):9–14, 2008.
59. T. Brys. *Extraction of ultracold neutrons from a solid deuterium source*. PhD thesis, ETH Zürich, No. 17350, 2007.
60. Abel, C. and N. J. Ayres, G. Ban, G. Bison, K. Bodek, V. Bondar, E. Chanel, P.-J. Chiu, M. Daum, S. Emmenegger, L. Ferraris-Bouchez, P. Flaux, W. C. Griffith P. G. Harris, N. Hild, Y. Kermaidic, K. Kirch, P. A. Koss, J. Krempel, B. Lauss, T. Lefort, Y. Lemièrè, A. Leredde, P. Mohanmurthy, M. Musgrave, O. Naviliat-Cuncic, D. Pais, F. M. Piegsa, G. Pignol, M. Rawlik, D. Rebreyend, D. Ries, S. Roccia, D. Rozpedzik, P. Schmidt-Wellenburg, A. Schnabel, N. Severijns, J. Thorne, R. Viro, J. Voigt, A. Weis, E. Wursten, J. Zejma, G. Zsigmond. nEDM experiment at PSI: data-taking strategy and sensitivity of the dataset. *arXiv.org*, 1811.04012, 2018.
61. Abel, C. and N. J. Ayres, G. Ban, G. Bison, K. Bodek, V. Bondar, E. Chanel, P.-J. Chiu, B. Clement, C. Crawford, M. Daum, S. Emmenegger, P. Flaux, L. Ferraris-Bouchez, W. C. Griffith, Z. D. Grujic, P. G. Harris, W. Heil, N. Hild, K. Kirch, P. A. Koss, A. Kozela, J. Krempel, B. Lauss, T. Lefort, Y. Lemièrè, A. Leredde, P. Mohanmurthy, O. Naviliat-Cuncic, D. Pais, F. M. Piegsa, G. Pignol, M. Rawlik, D. Rebreyend, D. Ries, S. Roccia, K. Ross, D. Rozpedzik, P. Schmidt-Wellenburg, A. Schnabel, N. Severijns, J. Thorne, R. Viro, J. Voigt, A. Weis, E. Wursten, J. Zejma, G. Zsigmond. The n2EDM experiment at the Paul Scherrer Institute. *arXiv.org*, 1811.02340, 2018.
62. M. Klein and Ch.J. Schmidt. CASCADE, neutron detectors for highest count rates in combination with ASIC/FPGA based readout electronics. *Nuclear Instrum. Methods A*, 628(1):9–18, 2011.
63. L. Göttl. Measurements and procedures for the construction and characterization of ultra-cold neutron guides. Master's thesis (Diplomarbeit), University of Heidelberg and University of Mainz, 2008.

64. J. Kahlenberg, D. Ries, K. U. Ross, C. Siemensen, M. Beck, C. Geppert, W. Heil, N. Hild, J. Karch, S. Karpuk, F. Kories, M. Kretschmer, B. Lauss, T. Reich, Y. Sobolev, and N. Trautmann. Upgrade of the ultracold neutron source at the pulsed reactor TRIGA mainz. *The European Physical Journal A*, 53(11):226–, 2017.
65. A. Steyerl. Effect of surface roughness on the total reflexion and transmission of slow neutrons. *Z. Phys. A*, 254:169–188, 1972. 10.1007/BF01380066.
66. Polish Grid Infrastructure, <http://www.plgrid.pl/en>.